

ECNS: Energy-Conserving Navier-Stokes Solver

Verification of steady laminar flows

B. Sanderse

Abstract

This report describes the verification of a second order ‘energy-conserving’ finite volume method, for the solution of the incompressible Navier-Stokes equations on staggered, cartesian grids. Four different test cases are examined, being channel flow, lid-driven cavity flow, backward-facing step flow and flow through an actuator disk. The accuracy of the spatial discretization is investigated by looking at laminar, steady flow. Second order accuracy is shown for velocity and pressure on uniform and non-uniform meshes, in 2D and 3D, and for different boundary conditions. In the case of flow through an actuator disk a discontinuity in the pressure is present, which is correctly captured by the method. The method is suitable to be extended to compute unsteady turbulent flows, such as the flow of air in wind turbine wakes.

Contents

| | | |
|-------|--|----|
| 1 | Introduction | 5 |
| 1.1 | Background | 5 |
| 1.2 | Investigating the spatial accuracy | 5 |
| 1.3 | Post-processing results | 6 |
| 1.4 | Outline of report | 6 |
| 2 | Channel flows | 7 |
| 2.1 | Couette flow | 7 |
| 2.1.1 | Introduction | 7 |
| 2.1.2 | Settings | 7 |
| 2.1.3 | Results | 7 |
| 2.2 | Poiseuille flow | 8 |
| 2.2.1 | Introduction | 8 |
| 2.2.2 | Settings | 8 |
| 2.2.3 | Results | 9 |
| 3 | Lid-driven cavity | 13 |
| 3.1 | Regularized lid-driven cavity | 13 |
| 3.1.1 | Introduction | 13 |
| 3.1.2 | Settings | 14 |
| 3.1.3 | Results | 14 |
| 3.2 | Original lid-driven cavity | 17 |
| 3.2.1 | Introduction | 17 |
| 3.2.2 | Settings | 17 |
| 3.2.3 | Results | 17 |
| 3.3 | 3D lid-driven cavity | 23 |
| 3.3.1 | Introduction | 23 |
| 3.3.2 | Settings | 23 |
| 3.3.3 | Results | 23 |
| 4 | Flow over a backward-facing step | 27 |
| 4.1 | Introduction | 27 |
| 4.2 | Settings | 27 |
| 4.3 | Results | 28 |
| 5 | Actuator disk model | 33 |
| 5.1 | Introduction | 33 |
| 5.2 | 1D | 33 |
| 5.3 | 2D lightly loaded, ‘inviscid’ | 34 |

| | | |
|-------|---|----|
| 5.3.1 | Introduction | 34 |
| 5.3.2 | Settings | 35 |
| 5.3.3 | Results | 35 |
| 5.4 | 2D heavily loaded, ‘inviscid’ | 41 |
| 5.5 | 2D heavily loaded, viscous | 41 |
| 5.6 | 3D lightly loaded | 45 |
| 5.6.1 | Introduction | 45 |
| 5.6.2 | Settings | 46 |
| 5.6.3 | Results | 46 |
| 5.7 | 3D heavily loaded, viscous | 49 |
| 5.7.1 | Introduction | 49 |
| 5.7.2 | Settings | 49 |
| 5.7.3 | Results | 49 |
| 6 | Conclusions | 53 |
| | References | 55 |

1 Introduction

1.1 Background

At the Energy research Center of the Netherlands (ECN) a computational fluid dynamics (CFD) code is developed for the computation of wind turbine wakes in large wind farms: Energy-Conserving Navier-Stokes Solver (ECNS). This report describes a number of benchmark cases to verify the spatial discretization. *Verification* means that we investigate if we *solve the equations right*, i.e. we are not concerned here if we solve the right equations (known as validation). We are focusing on *steady, laminar, incompressible* flow, i.e. we solve the following set of equations:

$$\nabla \cdot \mathbf{u} = 0, \quad (1)$$

$$(\mathbf{u} \cdot \nabla)\mathbf{u} = -\nabla p + \frac{1}{\text{Re}}\nabla^2\mathbf{u} + \mathbf{F}, \quad (2)$$

where \mathbf{u} is the velocity, p the pressure and \mathbf{F} a body force, all non-dimensionalized with a reference length L , density ρ_∞ and velocity u_∞ ; the Reynolds number is $\text{Re} = u_\infty L/\nu$.

ECNS solves equations (1) and (2) with a second order accurate finite volume method on a staggered cartesian grid, based on the original method of Harlow and Welch [12]. Both the convective and diffusive terms are approximated by central differences; this results in a ‘symmetry-preserving’ discretization [20] that conserves discretely the kinetic energy of the flow in the absence of boundaries, viscosity and body forces. The system of non-linear equations that results from the spatial discretization is solved with a direct solver from Matlab (if not indicated otherwise). Although this system is a singular saddle-point system, we have not found any major difficulties in obtaining accurate and converged results. Of course, a direct solver is not of interest for many practical problems, but here the focus is on testing the accuracy of the spatial discretization and not on the most efficient way of solving the system of equations.

1.2 Investigating the spatial accuracy

The error associated with the numerical solution of (1)-(2) can be written as follows:

$$e = \|\mathbf{u} - \mathbf{u}^h\|, \quad (3)$$

where $\|(\cdot)\|$ indicates a suitable norm, \mathbf{u} the exact (discrete) solution, and \mathbf{u}^h the approximate (discrete) solution. e can be divided into several components:

$$e = e_d + e_i + e_r, \quad (4)$$

where

- e_d : (spatial) discretization error,
- e_i : iterative error, resulting from the solution of the non-linear system of equations,
- e_r : round-off error.

There is no temporal discretization error and no turbulence modeling error, because we solve the steady laminar equations. We iterate until $e_i \ll e_d$, so with the assumption that $e_r \ll e_d$ we effectively investigate the spatial discretization error. The expected second order spatial accuracy of the scheme can then be expressed as

$$e \approx e_d = \mathcal{O}(h^2). \quad (5)$$

1.3 Post-processing results

When showing results in this report, variables are plotted at the position where they are naturally defined on a staggered grid, see figure 1. The total velocity $V = \sqrt{u^2 + v^2}$ is defined at the center of a pressure finite volume, u and v at its faces. The vorticity follows from the velocity as

$$\boldsymbol{\omega} = \nabla \times \mathbf{u}, \quad (6)$$

which reads in two dimensions $\omega_z = \frac{\partial v}{\partial x} - \frac{\partial u}{\partial y}$, so it is naturally defined at the corners of a pressure finite volume. The streamfunction ψ is mainly used in two dimensions and in that case defined by $\mathbf{u} = \nabla \times (\psi_z \hat{\mathbf{e}}_z)$. It can be found by solving a Poisson equation,

$$\nabla^2 \psi_z = -\omega_z, \quad (7)$$

and is, like the vorticity, defined at the corners of a pressure finite volume.

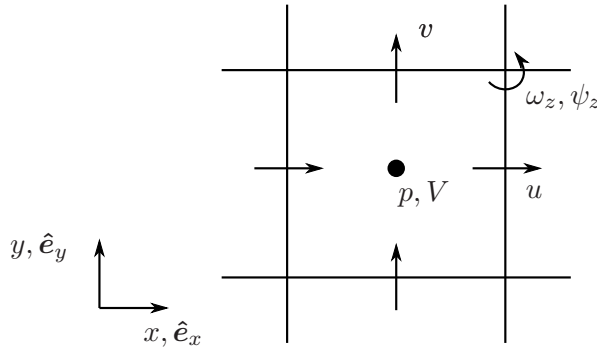


Figure 1: Staggered grid layout with p -centered control volume.

1.4 Outline of report

Four different ‘types’ of flow are considered in this report. Firstly, section 2 discusses channel flows with analytical solutions: Couette and Poiseuille flow. Secondly, in section 3 we investigate the regularized and classical lid driven-cavity flow, in both 2D and 3D. Thirdly we examine the flow over a backward-facing step in section 4, which involves an investigation of outflow boundary conditions. Lastly, we consider an actuator disk in two and three dimensions in section 5, being an important test case for wind turbine wake applications.

2 Channel flows

In this section we discuss Couette and Poiseuille flow, two types of flow for which an analytical solution is available.

2.1 Couette flow

2.1.1 Introduction

Couette flow concerns the shear-driven flow between two horizontal plates, see figure 2. The x -momentum equation simplifies to $\frac{d^2 u}{dy^2} = 0$, so that the velocity profile is linear in y and independent of x :

$$u^{\text{exact}}(y) = U \frac{y}{H}, \quad (8)$$

with H the distance between the plates and U their velocity difference; here we set the velocity of the lower plate to 0 and the upper plate to U . The solution is independent of the Reynolds number. The y -momentum equation reduces to $\frac{dp}{dy} = 0$, meaning that the pressure is only a function of x , but since there is no driving pressure gradient the pressure is constant everywhere.

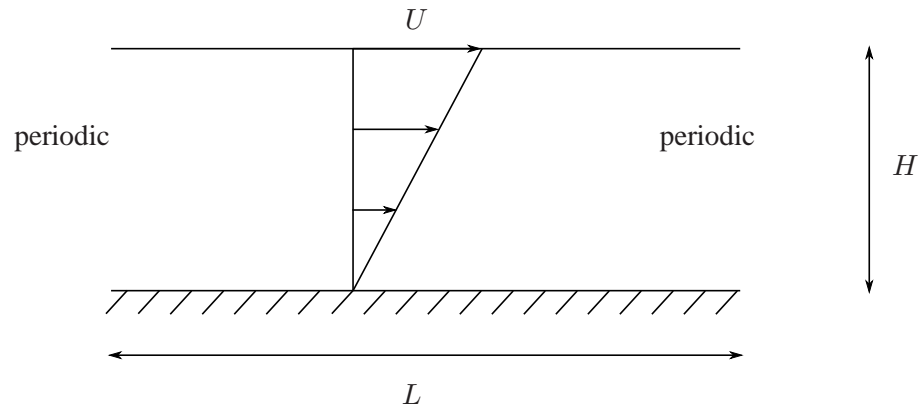


Figure 2: Couette flow.

2.1.2 Settings

The parameter values for this test are shown in table 1. We use periodic boundary conditions in the streamwise direction and Dirichlet condition on the upper and lower side. Other possible boundary conditions, such as inflow and outflow, will be considered in section 4 when dealing with the backward-facing step problem.

| parameter | value |
|-----------|-------|
| H | 1 |
| L | 1 |
| U | 1 |

Table 1: Settings for Couette flow.

2.1.3 Results

Since the exact solution is a linear velocity profile, it is expected that a discretization that has at least a first order *local* truncation error can represent this profile without any discretization error.

Indeed it was found that the numerical solution is within machine accuracy of the exact solution, for uniform and non-uniform grids, arbitrary H and L , number of cells, and boundary conditions. An example for $N_x = N_y = 10$ is shown in figure 3. The total velocity $V = \sqrt{u^2 + v^2}$ is shown here; it is defined at pressure locations so that the contour lines do not extend up to the boundaries. However, the fact that this linear velocity profile can be captured exactly does not prove that the local error is indeed at least first order. This will be explained in section 2.2.

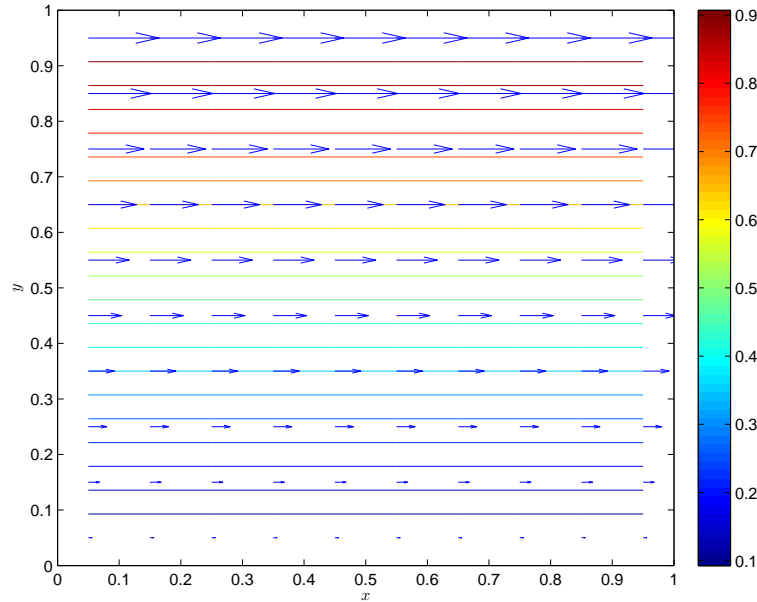


Figure 3: Velocity vectors and contour lines of total velocity for Couette flow.

2.2 Poiseuille flow

2.2.1 Introduction

The Poiseuille flow is the flow between two stationary plates driven by a pressure gradient. The x -momentum equation simplifies to:

$$\frac{1}{\text{Re}} \frac{d^2 u}{dy^2} = \frac{dp}{dx} = \text{const.} \quad (9)$$

After integrating and applying no-slip boundary conditions at $y = 0$ and $y = H$ we obtain the exact solution:

$$u^{\text{exact}}(y) = \frac{1}{2} a y (y - H), \quad (10)$$

with $a = \text{Re} \frac{dp}{dx}$. A negative pressure gradient is necessary for a positive velocity. The maximum velocity occurs at $y = H/2$ and is denoted by $U = -\frac{1}{8} H^2 a$. Here we will take U such that the average velocity is 1, i.e. $\frac{1}{H} \int u dy = 1$, which gives $U = \frac{3}{2}$ and $a = -12/H^2$.

2.2.2 Settings

The parameters for this test are shown in table 2. The pressure gradient is applied as a constant body force in case of periodic boundary conditions. In case of inflow/outflow conditions no body

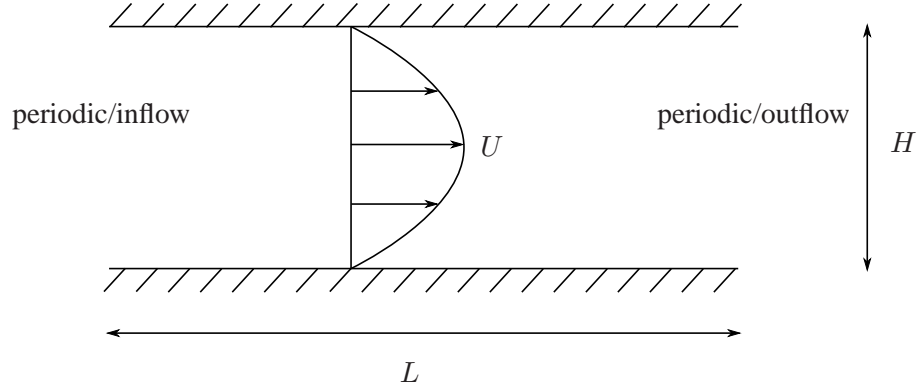


Figure 4: Poiseuille flow.

force has to be applied. The Reynolds number is not important for the results since it shows up both in the forcing term and in the diffusive terms (convective terms are zero). Two grids in y -direction will be investigated: uniform and cosine. In x -direction the number of grid points is not important, because the solution is independent of x for periodic boundary conditions. The cosine grid is given as a transformation of a uniform grid:

$$\frac{y^{\text{cosine}}}{H} = \frac{1}{2} \left(1 - \cos \left(\frac{\pi y^{\text{uniform}}}{H} \right) \right). \quad (11)$$

This type of grid has refinement near the boundaries and will later also be applied in the lid-driven cavity testcase in section 3.

| parameter | value |
|-----------------|------------------------|
| H | 1 |
| L | 2 |
| U | 3/2 |
| Re | 100 |
| $\frac{dp}{dx}$ | $-12/(\text{Re } H^2)$ |

Table 2: Settings for Poiseuille flow.

2.2.3 Results

Figures 5 and 6 show the solution in terms of velocity field and vectors at pressure locations on a uniform 10×20 grid with periodic boundary conditions. For these boundary conditions the solution is completely independent of x ; this is not the case when prescribing an inflow condition according to the exact solution, because the discretization scheme is not able to capture the quadratic solution exactly (on a uniform grid). This will be explained below.

In figure 7 we show the following errors:

$$e_2 = \left(\frac{1}{N_y} \sum_{i=1}^{N_y} |\epsilon_i|^2 \right)^{\frac{1}{2}}, \quad (12)$$

$$e_\infty = \max |\epsilon_i|, \quad (13)$$

where $\epsilon_i = u_i^h - u^{\text{exact}}(y_i)$ and u_i^h is the discrete numerical solution in point i on the mesh with grid size h . The global error is clearly second-order accurate on both the uniform and cosine

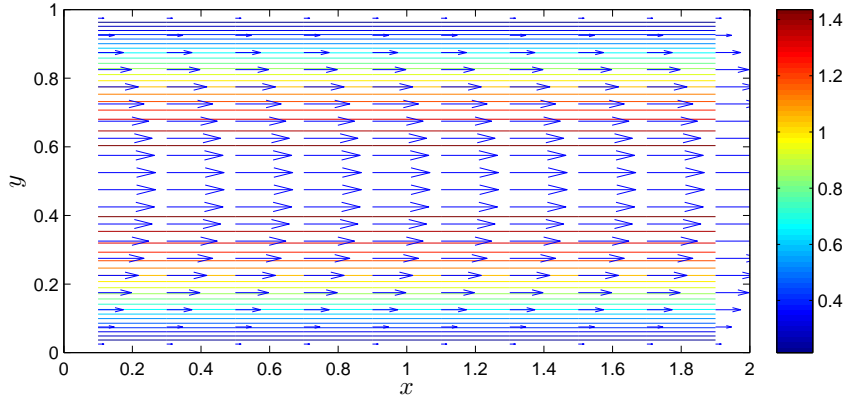


Figure 5: Velocity vectors and contour lines of total velocity for Poiseuille flow.

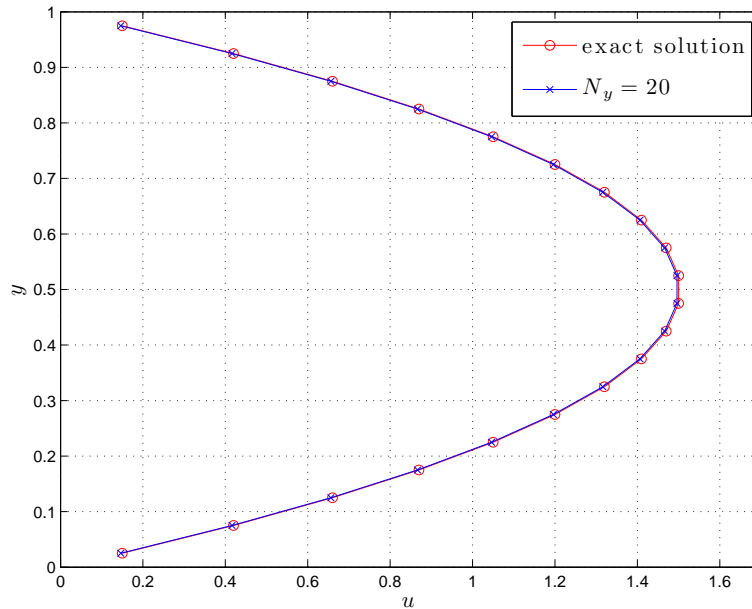


Figure 6: Numerical and exact solution for Poiseuille flow.

grid. However, the local error is not second-order accurate, because if that would be the case the solution would be represented exactly, as in the case of the Couette flow. The issue lies in the treatment of the boundary conditions. When performing Taylor expansions, it can be shown that the discretization scheme has a zeroth order (inconsistent!) *local* truncation error near boundaries:

$$u_{yy} \approx \frac{3}{4}u_{yy} + \mathcal{O}(\Delta y). \quad (14)$$

The inconsistency at the boundary error does not restrict the *global* error; it is ‘allowed’ to lose two orders of accuracy at the boundary without affecting the global error (see e.g. [21, 13]). In the Couette testcase this inconsistency did not show up because in that particular case $u_{yy} = 0$. The Couette testcase is therefore not suitable to draw conclusions on the local order of accuracy of the diffusive discretization.

Figure 7 shows that for uniform grids e_2 and e_∞ are equal, indicating that the error between numerical and exact solution is the same for all mesh points. This can be explained as follows.

The approximate solution u^h is the solution to

$$Du^h = \begin{pmatrix} a \\ a \\ \vdots \\ a \end{pmatrix}, \quad (15)$$

whereas the exact discrete solution satisfies

$$Du^{\text{exact}} = \begin{pmatrix} \tilde{a} \\ a \\ \vdots \\ \tilde{a} \end{pmatrix}. \quad (16)$$

Here D is the (symmetric) diffusion operator, and \tilde{a} is first order approximation to a , due to the fact that the discretization is first order at the boundaries. The global error e is then given by

$$e = u^h - u^{\text{exact}} \quad (17)$$

$$= D^{-1} \begin{pmatrix} a - \tilde{a} \\ 0 \\ \vdots \\ a - \tilde{a} \end{pmatrix} \quad (18)$$

$$= D^{-1}\tau, \quad (19)$$

where τ is the local error. D^{-1} smears out the (inconsistent) local error at the boundaries over the entire domain, leading to a second order global error. Since both D and D^{-1} are bi-symmetric (symmetric around both diagonals), and the first and last column of D^{-1} can be described by a linear function, one can find that

$$u_i^h - u_i^{\text{exact}} = \text{constant}, \quad (20)$$

in accordance with the results.

For the cosine grid the clustering of points near the walls leads to locally smaller errors, but the coarse and non-uniform spacing in the center lead to large errors in that region, so that overall the cosine mesh is less accurate than the uniform mesh. In all cases we observe second order convergence upon mesh refinement. This is important, because in many practical flow problems non-uniform grids are used (e.g. boundary layer flows), and it is then good to still have second-order convergence. However, since many terms in the Navier-Stokes equations are zero for this test case (the vertical velocity component v and all derivatives in x -direction), it is too early to conclude that the discretization is second order accurate. For this we move to a more complex flow situation.

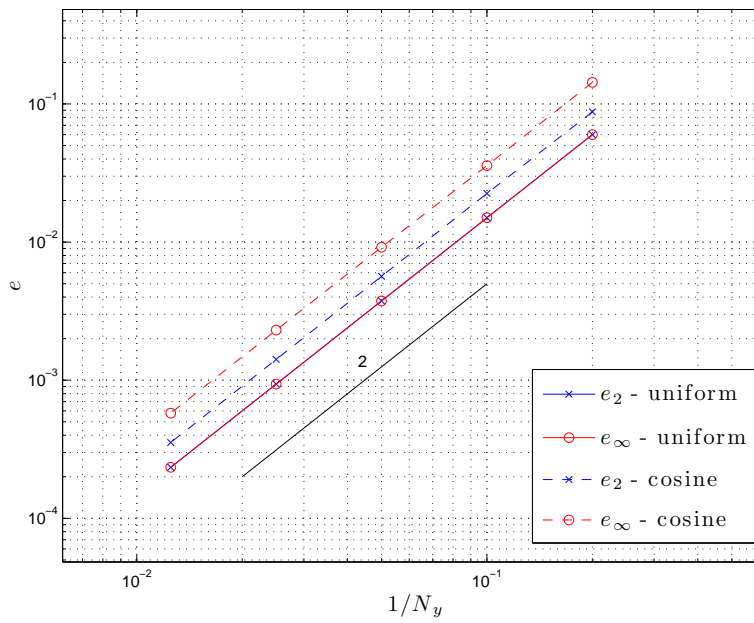


Figure 7: Convergence of errors in different norms and for different grids for Poiseuille flow.

3 Lid-driven cavity

The lid-driven cavity flow is a widely used benchmark problem for the incompressible Navier-Stokes equations. It combines a simple Cartesian geometry and no-slip boundary conditions with complicated flow patterns, such as separating boundary layers and recirculation regions, which become increasingly difficult to compute as the Reynolds number is increased. The classical lid-driven cavity has a lid moving with constant velocity, having singularities in the upper left and upper right corners, where one can question the validity of discretization error studies because Taylor expansions might not be well-defined. In order to circumvent this problem we first test a regularized cavity before moving to the original problem.

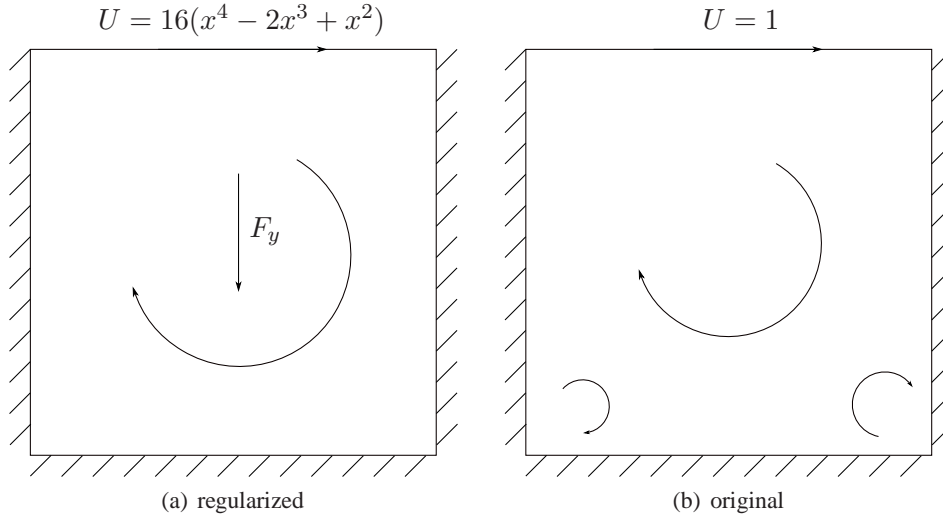


Figure 8: Lid-driven cavity.

3.1 Regularized lid-driven cavity

3.1.1 Introduction

The regularized lid-driven cavity, defined on a domain $[0, 1] \times [0, 1]$ has a lid whose horizontal velocity is $U = 16(x^4 - 2x^3 + x^2)$, resulting in a zero velocity in the upper-left and upper-right corners. Furthermore, it is possible to obtain an exact solution for the velocity and pressure field by *choosing* a solution that satisfies the boundary conditions and then introducing a body force, $\mathbf{F} = F_y \hat{\mathbf{e}}_y$, such that the Navier-Stokes equations are satisfied; this is known as the method of manufactured solutions. Shih et al. [17] choose the following velocity and pressure field:

$$u(x, y) = 8(x^4 - 2x^3 + x^2)(4y^3 - 2y), \quad (21)$$

$$v(x, y) = -8(4x^3 - 6x^2 + 2x)(y^4 - y^2), \quad (22)$$

$$p(x, y) = \frac{8}{\text{Re}}(H_1(x)g'''(y) + h(x)g'(y)) + 64H_3(x)(g(y)g''(y) - (g'(y))^2). \quad (23)$$

Substitution into the Navier-Stokes equations leads to the following body force:

$$F_y = \frac{8}{\text{Re}}(24H_1(x) + 2h'(x)g''(y) + h'''(x)g(y)) + 64(H_3(x)G_1(y) - g(y)g'(y)H_2(x)), \quad (24)$$

where

$$h(x) = x^4 - 2x^3 + x^2, \quad (25)$$

$$H_1(x) = \frac{1}{5}x^5 - \frac{1}{2}x^4 + \frac{1}{3}x^3, \quad (26)$$

$$H_2(x) = -4x^6 + 12x^5 - 14x^4 + 8x^3 - 2x^2, \quad (27)$$

$$H_3(x) = \frac{1}{2}(x^4 - 2x^3 + x^2)^2, \quad (28)$$

$$g(y) = y^4 - y^2, \quad (29)$$

$$G_1(y) = -24y^5 + 8y^3 - 4y. \quad (30)$$

Primes ' denote differentiation with respect to the independent variable. As implementation check Shih et al. provide the value of F_y at the center of the cavity at $\text{Re} = 1$: $F_y(0.5, 0.5) = -3.356250$. Note that Shih et al. use $-F_y$ in the Navier-Stokes equations and as a result (24) also has an additional minus sign. The velocity component u is symmetric around $x = 0.5$, the v -component is anti-symmetric around $x = 0.5$; both are independent of Re . The sequence of vortices that appear in the lower right and lower left corner in the classical lid-driven cavity are not present here.

3.1.2 Settings

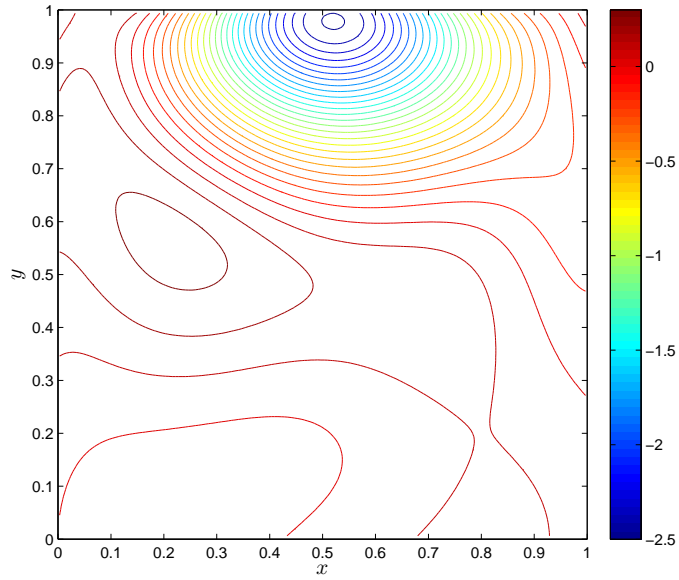
The domain is a cavity defined on $[0, 1] \times [0, 1]$. The initial condition is a zero velocity and pressure field. The Reynolds number is $\text{Re} = 100$. For the convergence of the solution we require that the maximum residual has dropped below 10^{-12} ; it might be better to put a condition on the *drop* in the initial residual, but on the other hand the initial residual depends on the initial guess. The first 3 steps are performed with Picard iteration, which provides a good starting value for subsequent Newton iterations. The mesh is uniform for all simulations.

| parameter | value |
|-------------|------------------------|
| U | $16(x^4 - 2x^3 + x^2)$ |
| Re | 100 |
| N_x, N_y | 10, 20, \dots , 160 |

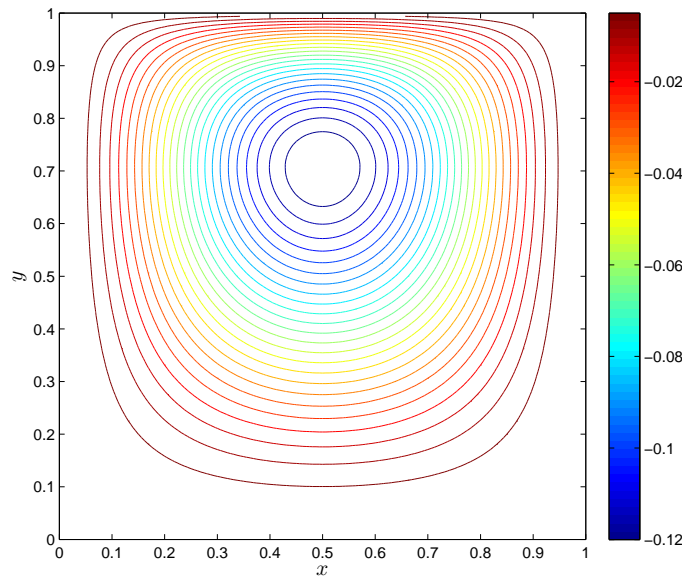
Table 3: Settings for regularized lid-driven cavity flow.

3.1.3 Results

Figure 9 shows the body force field F_y and the streamfunction ψ from a computation with a uniform grid with $N_x = N_y = 160$. Errors are calculated for different uniform grids in the same way as equations (12) and (13) with N_y replaced by $N = N_x N_y$. For calculating the error in the pressure we add a constant to the calculated pressure such that it is equal to the exact solution in the lower left grid point ($p_{1,1}^h = p^{\text{exact}}(x_1, y_1)$). This is valid, because the pressure in the incompressible Navier-Stokes equations is determined up to a constant in case of Dirichlet boundary conditions for the velocity on the entire boundary. Figure 10 shows that both velocity and pressure are second order in the L_2 - and L_∞ -norms. The convergence of the maximum residual is shown to be basically independent of the number of grid points, see figure 11. The initial residual, corresponding to the initial guess, is not shown in this figure. After a slow initial decrease in residual, corresponding to Picard iteration, quadratic convergence follows, corresponding to Newton's method.



(a) Force field, contour lines $-2.5 \dots 0.5$ with steps 0.1



(b) Streamfunction, contour lines $-0.12 \dots 0$ with steps 0.005

Figure 9: Force and streamfunction on uniform grid, $N_x = N_y = 160$, for regularized lid-driven cavity flow.

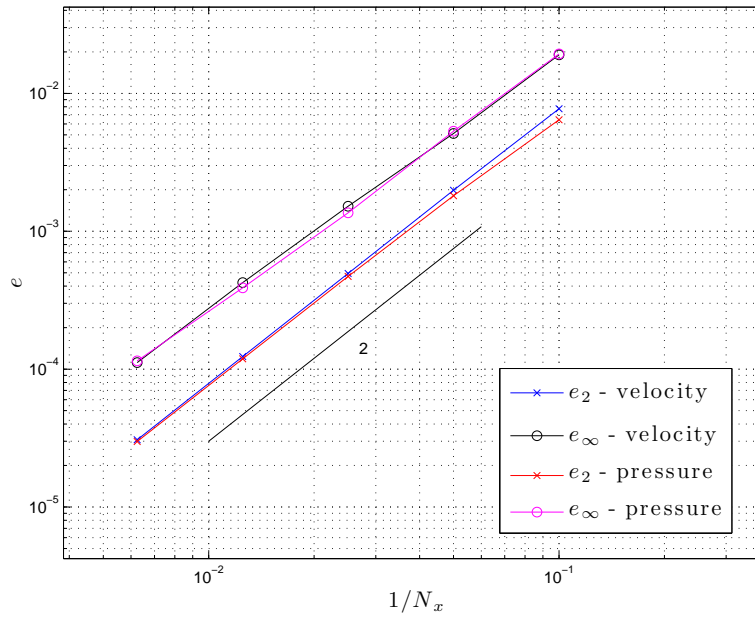


Figure 10: Convergence of errors in different norms for velocity and pressure for regularized lid-driven cavity flow.

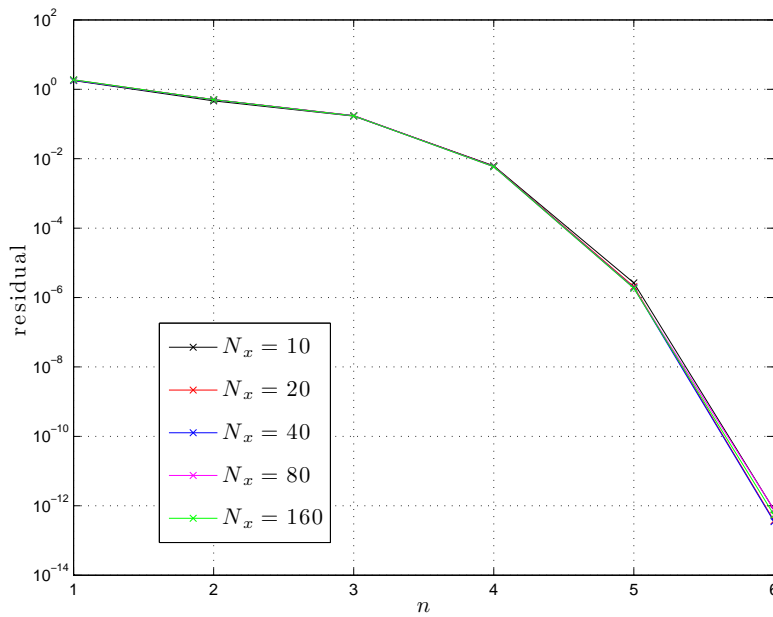


Figure 11: Convergence of residual for different grid sizes for regularized lid-driven cavity.

3.2 Original lid-driven cavity

3.2.1 Introduction

The original lid-driven cavity is shown in figure 8(b). Depending on the Reynolds number, a sequence of vortices is formed in the lower left and lower right corners. The classic benchmark paper on this subject is from Ghia et al. [10], but since this paper more accurate results have been published, in particular the spectral data from Botella & Peyret [3].

3.2.2 Settings

The Reynolds number is $Re = 1000$ for all order studies. At higher Reynolds numbers only quantitative flow field pictures are given. The mesh is either uniform or cosine, given by equation (11). An example of such a mesh with $N_x = N_y = 16$ is shown in figure 12. The non-linear system of equations is started with a zero velocity field and solved with Picard (first 3 steps) and Newton (subsequent steps) iteration, like in the regularized lid-driven cavity case. The stopping criterion is 10^{-10} based on the reduction of the maximum residual of the second iteration step. This approach worked fine for the cosine meshes, but for coarse uniform grids, where the mesh Péclet number is much larger than 2 (this is especially important near solid boundaries), the residual would not converge. We then added a small constant (10^{-8}) to the diagonal of the saddle-point matrix for $N_x = 16$ and $N_x = 32$ which would lead to converged solutions. Since the equations are solved in ‘update’ or ‘delta’ form such an adaptation is allowed, because the iteration matrix does not influence the converged result, only the convergence rate. Furthermore we increased the number of Picard iterations to 6, and we changed the initial guess to $u = 1$, $v = 0$.

| parameter | value |
|------------|--------------------|
| U | 1 |
| Re | 1000, 5000, 10000 |
| N_x, N_y | 16, 32, \dots, 256 |

Table 4: Settings for original lid-driven cavity flow.

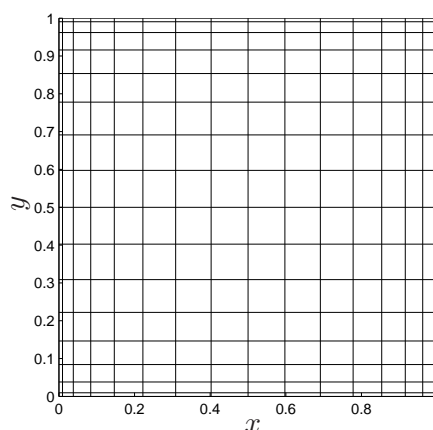


Figure 12: Nonuniform cosine mesh, 16×16 .

3.2.3 Results

Qualitatively the flow field is shown in figures 13(a)-13(c), obtained on a 256×256 cosine grid. These figures are indistinguishable from the benchmark results of [3], shown in figures 13(d)-

13(f).

The order of accuracy will be demonstrated in two ways: the convergence of the velocity profiles along the centerline and the convergence of the total kinetic energy in the cavity.

Firstly, we look at the velocity and the pressure profiles along the centerlines, see figures 14(a)-14(d). The pressure has been shifted such that $p = 0$ in the center of the cavity. Where necessary the velocity profiles of Botella & Peyret [3] have been mirrored because they use a lid with velocity $U = -1$. The grids with $N_x = N_y = 64$ and larger match the benchmark data very well. In order to measure the order of accuracy we compare the minimum value of u and maximum and minimum values of v along these centerlines with the benchmark data. Since the grid is relatively coarse in the center of the cavity (much coarser than the average grid spacing $1/N_x$), we approximate the centerline velocity profiles by fitting a spline through the data points, which is subsequently used to determine the minimum and maximum values and their locations. Especially the prediction of the location of minimum and maximum was improved in this way; the values itself are hardly affected. Second order behavior of the error between the values predicted by [3] ($u_{\min} = 0.3886$, $v_{\min} = -0.5270$, $v_{\max} = 0.3769$) and our results is shown in figure 15(a).

Secondly, we look at the total energy of the flow in the cavity:

$$k = \sum_{i,j} \frac{1}{2} V_{i,j}^2 \Omega_{i,j}, \quad (31)$$

where $\Omega_{i,j}$ is the area of a pressure finite volume, and $V_{i,j}^2 = (\frac{1}{2}(u_{i,j} + u_{i-1,j}))^2 + (\frac{1}{2}(v_{i,j} + v_{i,j-1}))^2$ ¹. We compare this value with the value reported in Bruneau & Saad [4], which is 0.044503 for $Re = 1000$. Figure 15(b) shows second order convergence for both the uniform and cosine mesh, but the cosine mesh has a lower error constant since it is better able to capture the boundary layers and corner vortices.

The convergence of the maximum residual is shown in figure 16. It is seen that the convergence behavior is basically independent of the grid size. The increase in initial residual with finer meshes is due to the fact that the initial velocity field is not smooth at the boundaries, leading to large gradients near boundaries and consequently a large residual. These gradients become larger for finer meshes. In all cases the uniform grids take more (Picard) iterations, a more careful initial guess and tuning to obtain convergence, compared to the cosine grid. A heuristic explanation for this behavior is that if the mesh Péclet number is smaller than 2, the upper-left block of the saddle-point matrix becomes a K -matrix, which improves the convergence behavior (see e.g. Wesseling [21]).

At higher Reynolds numbers more eddies are formed in the corners. The results for $Re=5000$ and $Re=10000$, presented in figure 17, compare very well to those presented in Erturk et al. [7]. In these cases we used 25 Picard iterations after which Newton iteration converged in a few steps. As a side note, it is interesting to see that Bruneau & Saad [4] disagree with the results of Erturk and mention that at a Reynolds number of 10000 the flow is not steady anymore. We will not go deeper into this discussion but just mention that we were able to obtain steady results as long as the grid was fine enough (128×128 in this case); these findings are also supported in Erturk [6].

¹An alternative definition, which agrees up to second-order accuracy, is $k = u^T \Omega^u u + v^T \Omega^v v$.

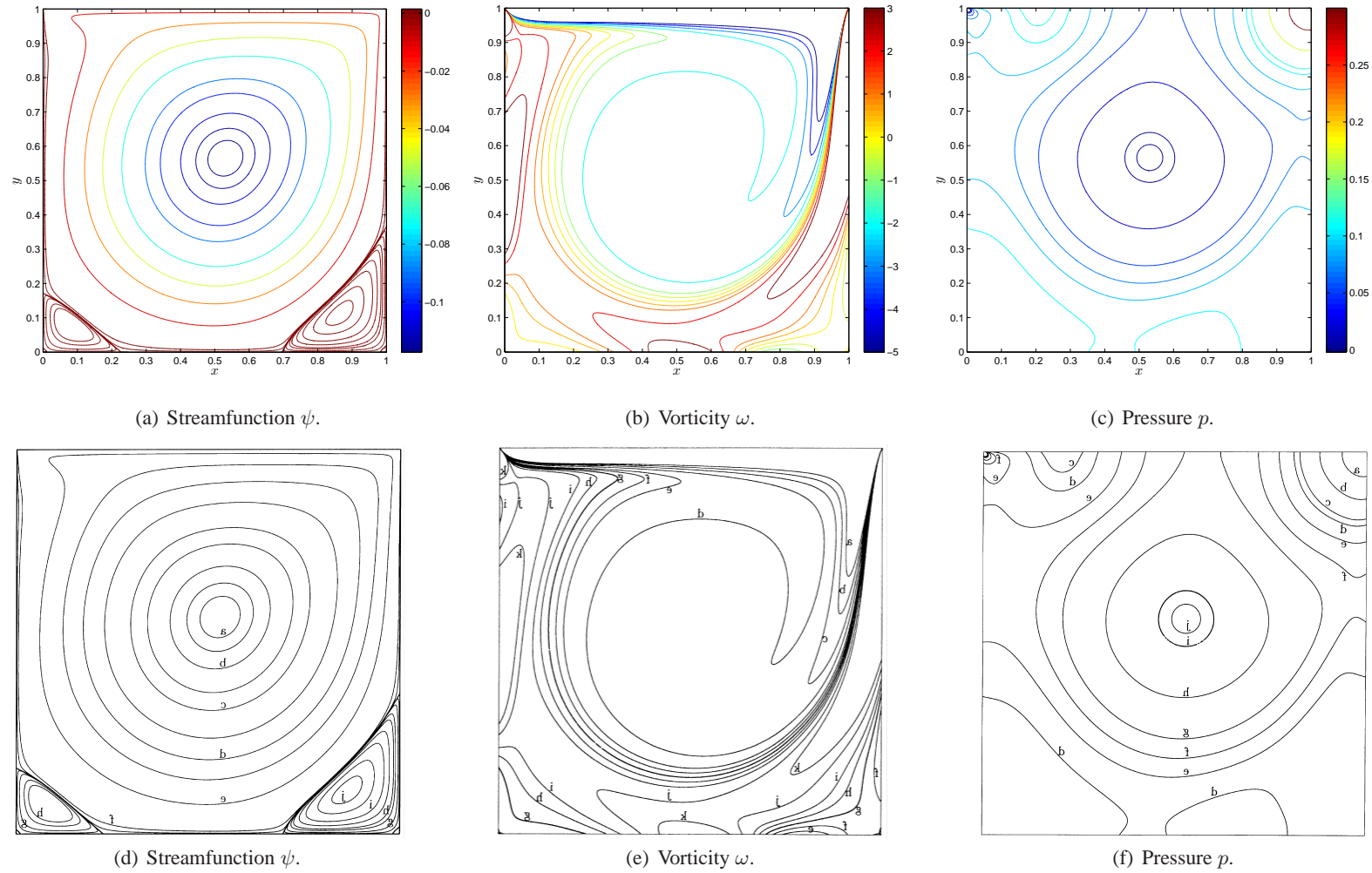


Figure 13: Contour plots for the lid-driven cavity flow at $Re=1000$. Upper row: current (non-uniform cosine mesh, 256×256); lower row: Botella & Peyret [3]. For contour line values see [3].

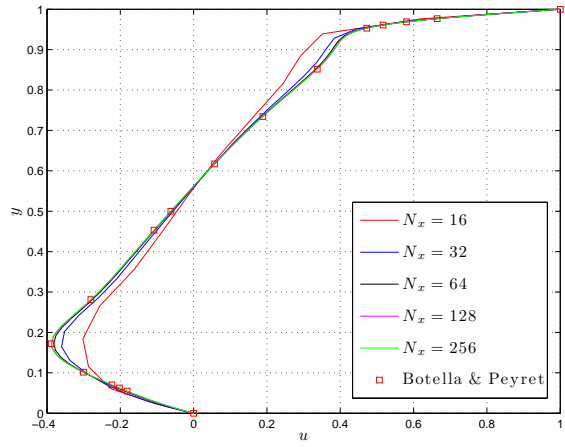
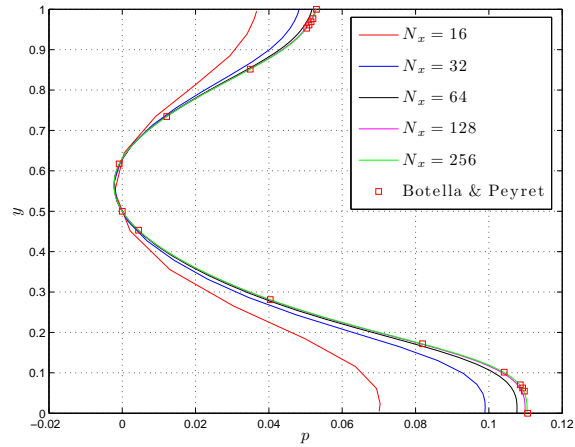
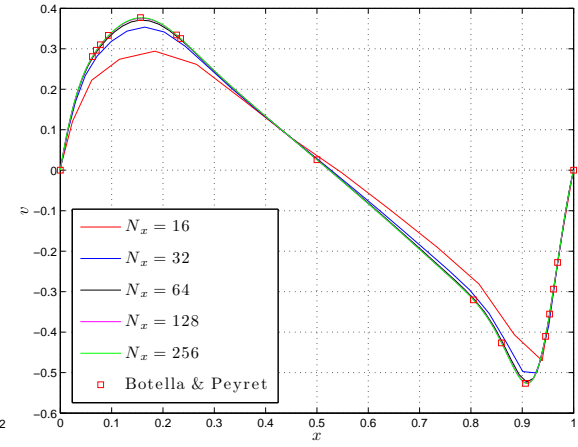
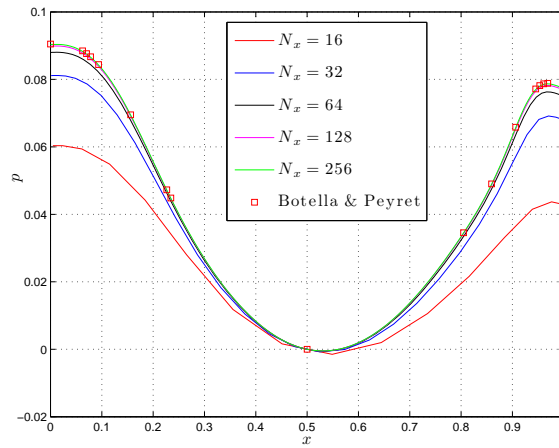
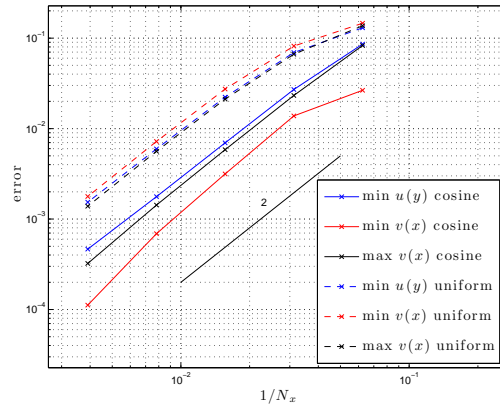
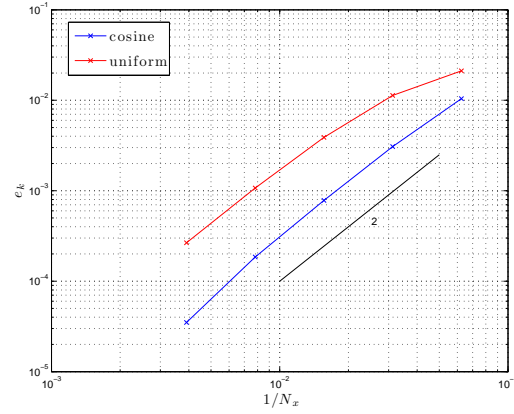
(a) u -profile along $x = 0.5$.(b) p -profile along $x = 0.5$.(c) v -profile along $y = 0.5$.(d) p -profile along $y = 0.5$.

Figure 14: Velocity and pressure profiles across the centerlines of the cavity for non-uniform cosine meshes.

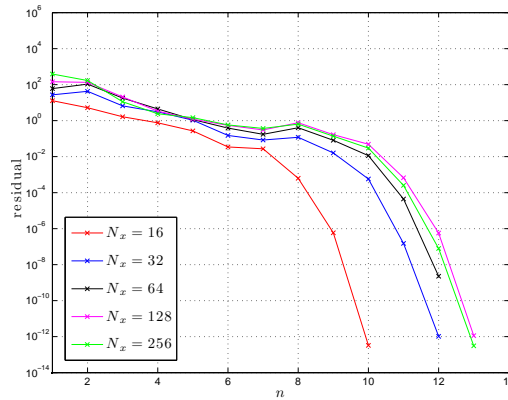


(a) Errors in velocity profiles.

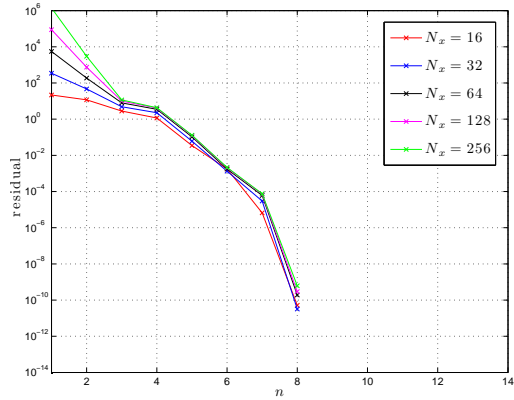


(b) Errors in kinetic energy.

Figure 15: Spatial convergence for uniform and cosine meshes.

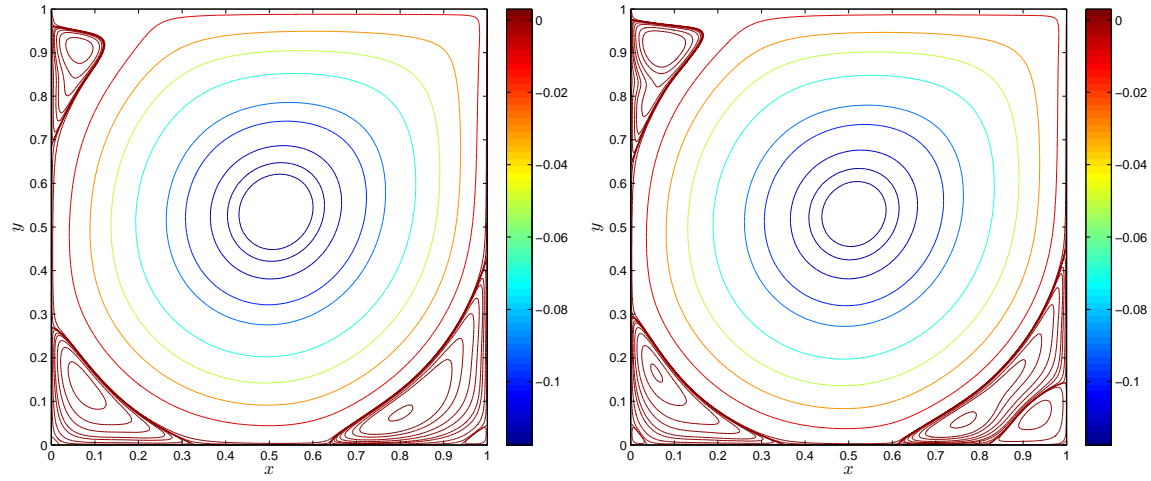
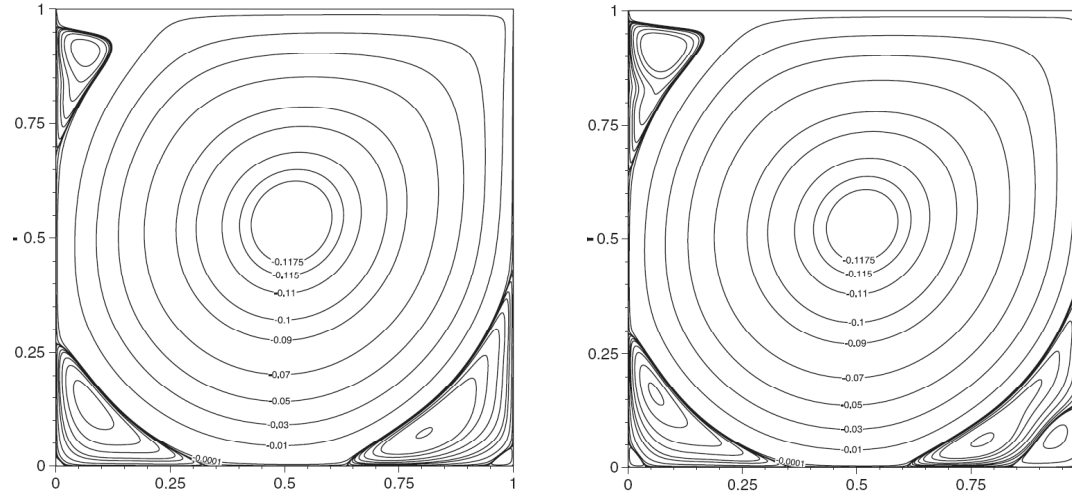


(a) uniform mesh



(b) cosine mesh

Figure 16: Convergence of maximum residual for different grids.

(a) Present results, $Re = 5000$.(b) Present results, $Re = 10,000$.(c) Erturk [7], $Re = 5000$.(d) Erturk [7], $Re = 10,000$.Figure 17: Streamfunction for higher Reynolds numbers, 128×128 cosine mesh. For contour line values see [7].

3.3 3D lid-driven cavity

3.3.1 Introduction

In three dimensions the lid-driven cavity flow exhibits complicated three-dimensional flow patterns and, when the Reynolds number is high enough, turbulence. As benchmark data we use the results of Albensoeder and Kuhlmann [1], who report accurate values of velocity profiles at $Re = 1000$ for rectangular cavities with different aspect ratios by employing a Chebyshev collocation method. Here we will consider only a cubical cavity.

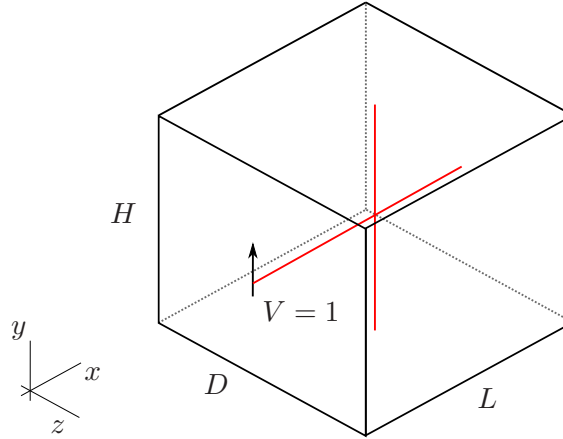


Figure 18: Three dimensional lid-driven cavity. The lid moves in y -direction. Velocity profiles are extracted along the red lines.

3.3.2 Settings

The same configuration as in [1] is used. The cavity has size $1 \times 1 \times 1$, and is defined on a domain $[-\frac{1}{2}, \frac{1}{2}] \times [-\frac{1}{2}, \frac{1}{2}] \times [-\frac{1}{2}, \frac{1}{2}]$. A cosine mesh (equation (11)) is used in all directions, where 1.5 times more volumes in x - and y -direction are used than in z -direction. The initial velocity field is $u = 1, v = 0, w = 0$; it was found by trial and error that this choice gave convergence with only 5 Picard iterations, while for other choices such as $u = 0, v = 1, w = 0$ or $u = v = w = 0$ it was considerably more difficult to obtain convergence. For these 3D computations it might be better to switch to a time-marching technique, as will be done in section 5.6, requiring significantly lower memory resources.

| parameter | value |
|-----------------------------|--------------------------|
| Re | 1000 |
| L | 1 |
| H | 1 |
| D | 1 |
| $N_x \times N_y \times N_z$ | $24 \times 24 \times 16$ |
| | $36 \times 36 \times 24$ |
| | $48 \times 48 \times 32$ |

Table 5: Settings for 3D lid-driven cavity flow.

3.3.3 Results

Qualitative pictures of the flow field are shown in figure 19. These figures are rotated compared to the sketch in figure 18. Figure 19(c) shows that the velocity in the center plane is very similar to

the two-dimensional case, see 13(a) and 13(a). However, important three-dimensional effects now occur, as can be seen from the streamlines that spiral inward to the center of the cavity. Outward going streamlines originate from the corner vortices, but have not been shown here for clarity reasons. More three-dimensional effects can be observed in figures 19(a) and 19(b); especially on the center planes $x = 0$ and $y = 0$ one observes the so-called Taylor-Görtler vortices.

A quantitative comparison is made in figures 20(a) and 20(b), where the velocity component v along the x -axis and the velocity component u along the y -axis of the cavity are plotted (see the red lines in figure 18). The error between our results and those of [1] is calculated by spline interpolation of our results to the position of the data points of [1], and then employing an L_2 -norm:

$$e = \left(\frac{1}{N} \sum_i^N |\bar{u}_i - u_i^{\text{AK}}|^2 \right)^{1/2}, \quad (32)$$

where \bar{u} indicates the interpolated data, u^{AK} indicates the data from [1].

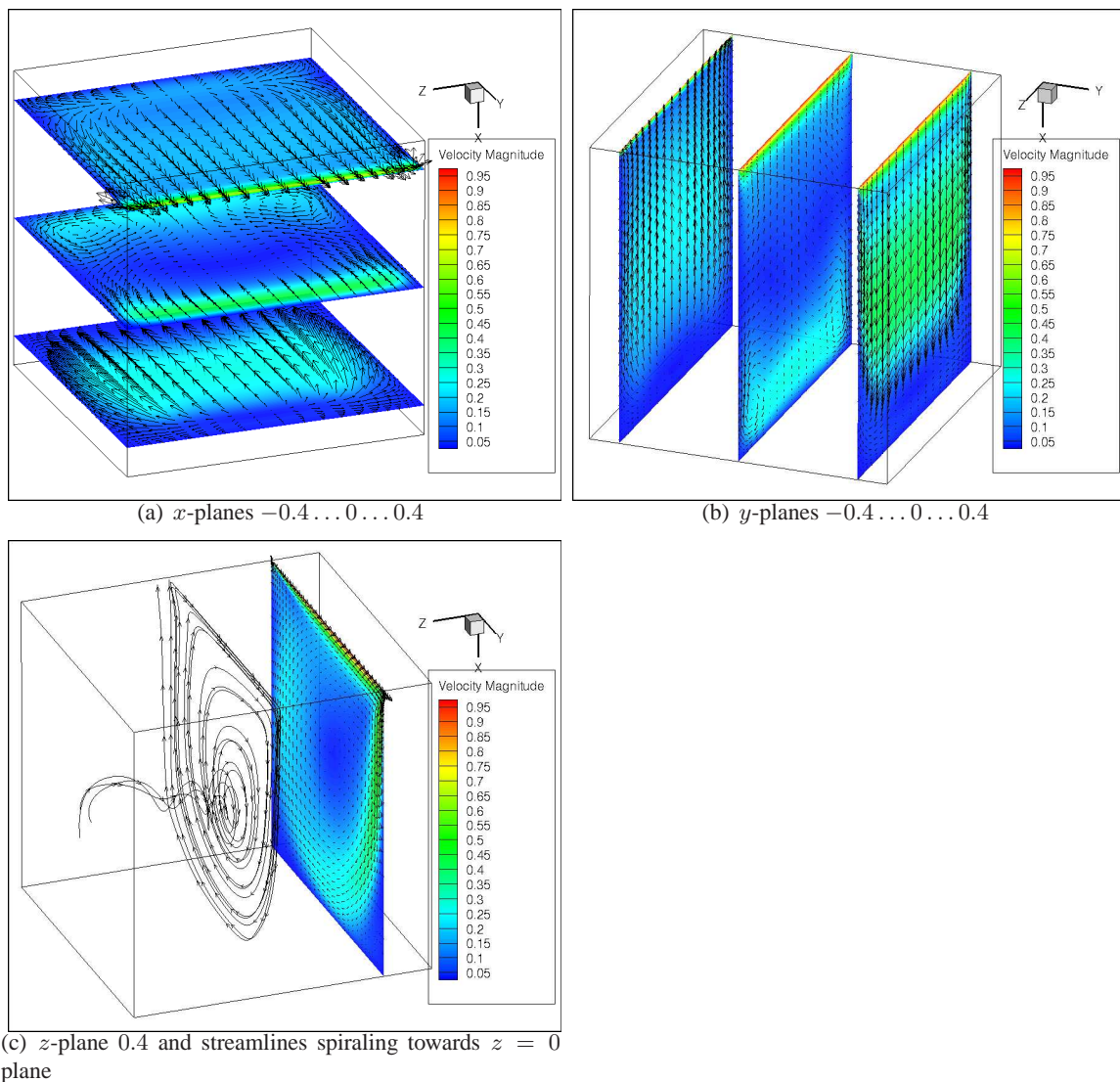
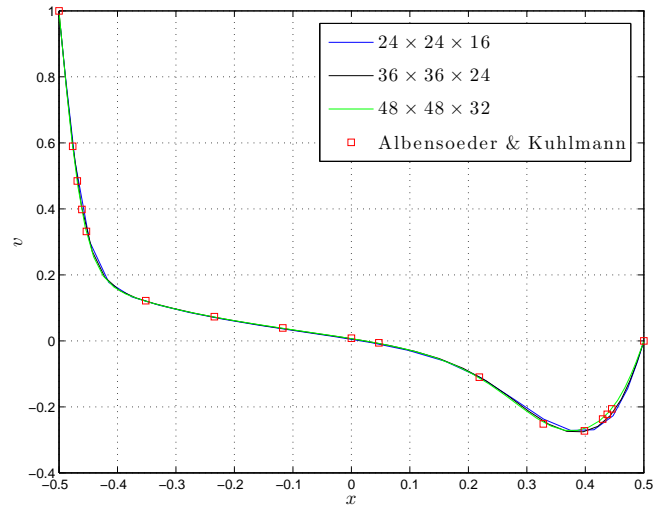
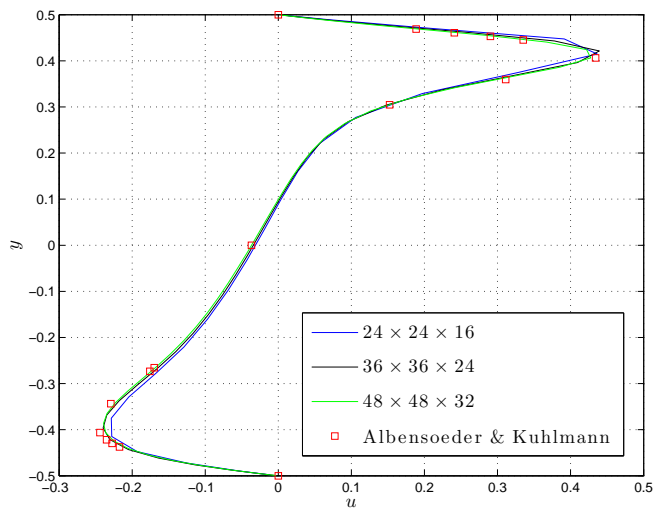


Figure 19: Qualitative pictures of velocity field, including vectors tangential to the slices, for the 3D lid-driven cavity.



(a) v along x -axis



(b) u along y -axis

Figure 20: Velocity profiles in 3D lid-driven cavity.

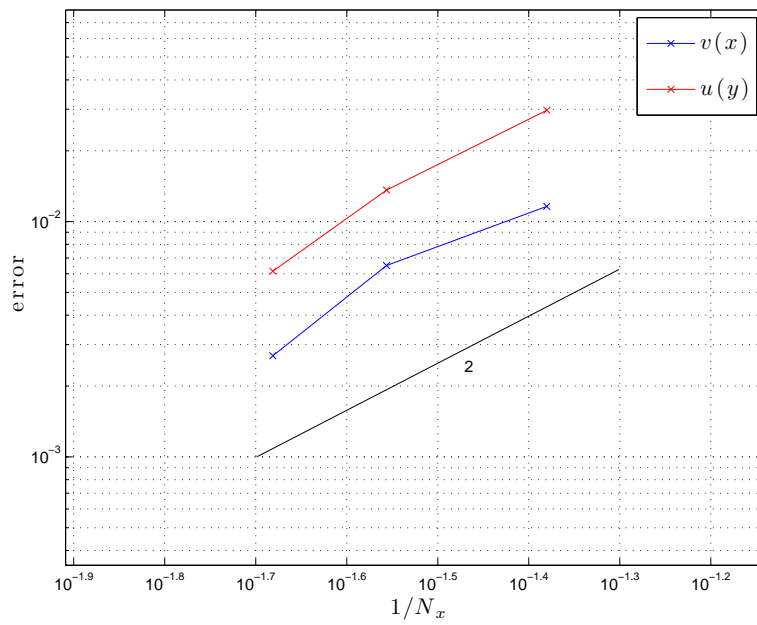


Figure 21: Error in velocity profiles as function of mesh size for 3D lid-driven cavity.

4 Flow over a backward-facing step

4.1 Introduction

The flow over a backward-facing step is performed to have a test problem with separating, reattaching and recirculating flow and to investigate the effect of outflow boundary conditions. The layout of the problem is shown in figure 22. Directly after the step a recirculation area forms along the lower bottom of the channel, which length X_1 increases with Reynolds number. Due to the downward deflection of the flow a second recirculation region appears on the upper side of the channel if the Reynolds number is large enough, characterized by X_2 and X_3 . The step is modeled by the prescription of a parabolic velocity profile at the inlet. The average value of this profile is $\bar{u} = 1$, its maximum is 1.5. The Reynolds number is based on the height of the channel and on \bar{u} : $\text{Re} = \bar{u}H/\nu$. An important issue is the treatment of outflow boundary conditions [9]; we will test here the outflow conditions:

$$p - \frac{1}{\text{Re}} \frac{\partial u}{\partial x} = p_\infty, \quad (33)$$

$$\frac{\partial v}{\partial x} = 0. \quad (34)$$

The results of Gartling [9] (at $\text{Re} = 800$) are believed to be accurate benchmark results for this problem and are therefore used as source of comparison. Erturk [5] also provides results on this test case, but in his work an inlet is added before the step, which results in a flow that is not perfectly parabolic at the step. An interesting article on the stability of the flow at $\text{Re} = 800$ is given in [11].

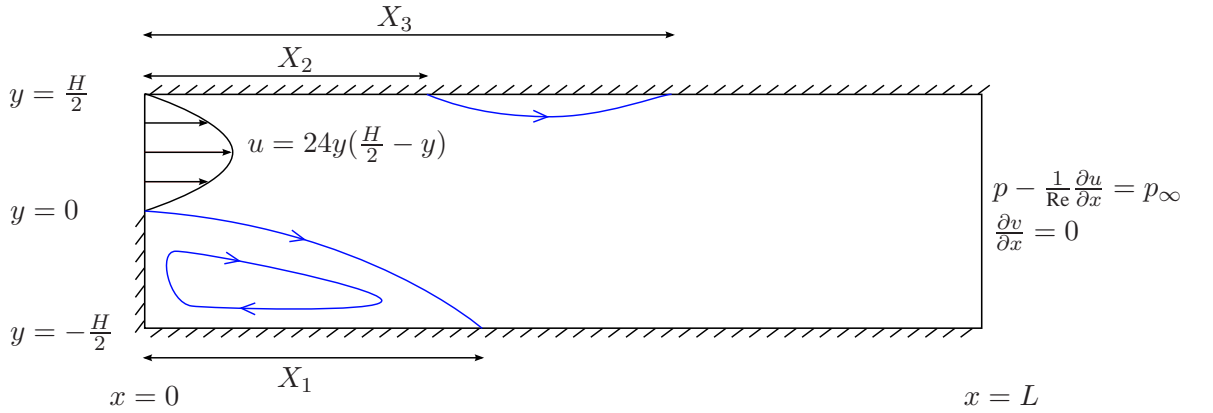


Figure 22: Layout for backward-facing step.

4.2 Settings

The value of the streamfunction at the lower wall is set at $\psi = 0$, the value at the upper wall follows from integrating $u(x=0, y)$ (given in figure 22):

$$\psi(x, y = \frac{H}{2}) = \int_{y=-H/2}^{y=H/2} u dy = \bar{u} \frac{H}{2}. \quad (35)$$

This gives the (Dirichlet) boundary condition for ψ used for solving equation (7). The reattachment points X_i are found at the point where $\frac{\partial u}{\partial y} = 0$, which can be found by tracking the $\psi = 0$ and $\psi = H/2$ contour lines to the boundary or looking for a change in the sign of u in the first

cell adjacent to the boundary.

At the end of the channel we set $p_\infty = 0$, but in order to compare with the results of Gartling [9], a constant was added to the pressure, as a post-processing step, so that $p = 0$ at the step corner ($x = 0, y = 0$); this constant is determined by interpolating the pressure values surrounding the corner. The non-linear system of equations is solved with 15 Picard iterations after which Newton iteration is applied.

For $L = 7.5$ and $L = 15$ uniform grids are used in x - and y -direction. For $L = 30$ the grid is stretched in x -direction, starting from $x = 15$ with a stretch factor of 1.005, resulting in a total of 1590×80 finite volumes.

| parameter | value |
|------------------|---|
| H | 1 |
| L | 7.5, 15, 30 |
| $N_x \times N_y$ | $600 \times 80, 1200 \times 80, 1590 \times 80$ |
| Re | 800 |
| p_∞ | 0 |

Table 6: Settings for backward-facing step flow.

4.3 Results

First we show qualitative pictures of the flow field by plotting streamfunction, pressure, vorticity and velocity contours, see figures 23(a)-23(d). The length of the domain used here is $L = 15$, but since physically interesting phenomena occur primarily for $x < 10$, the plots show the results until $x = 10$. Qualitatively these pictures match the results of [9] (figure 24) perfectly.

To test the outflow boundary condition we perform simulations on domains of different size and compare the velocity profiles at different streamwise sections with those of Gartling [9]. In figure 25(a) the velocity profiles at $x = 7$ are shown for $L = 7.5, L = 15$ and $L = 30$. It can be seen that even for $L = 7.5$, where *the domain cuts through the upper recirculation area*, the prediction of the velocity profile is still very good. The profiles obtained with $L = 15$ and $L = 30$ are visually indistinguishable from the results of Gartling. The same conclusions hold at $x = 15$. At $x = 30$ the flow has almost reached the form of the fully developed Poiseuille profile, see figure 25(c).

We continue with a study of the effect of the mesh size on X_1, X_2 and X_3 . We compute the error in X_i by comparing with the values provided by Gartling [9]: $X_1 = 6.10, X_2 = 4.85, X_3 = 10.48$. In figure 27 it can be seen that in all cases the error decreases with second order upon mesh refinement.

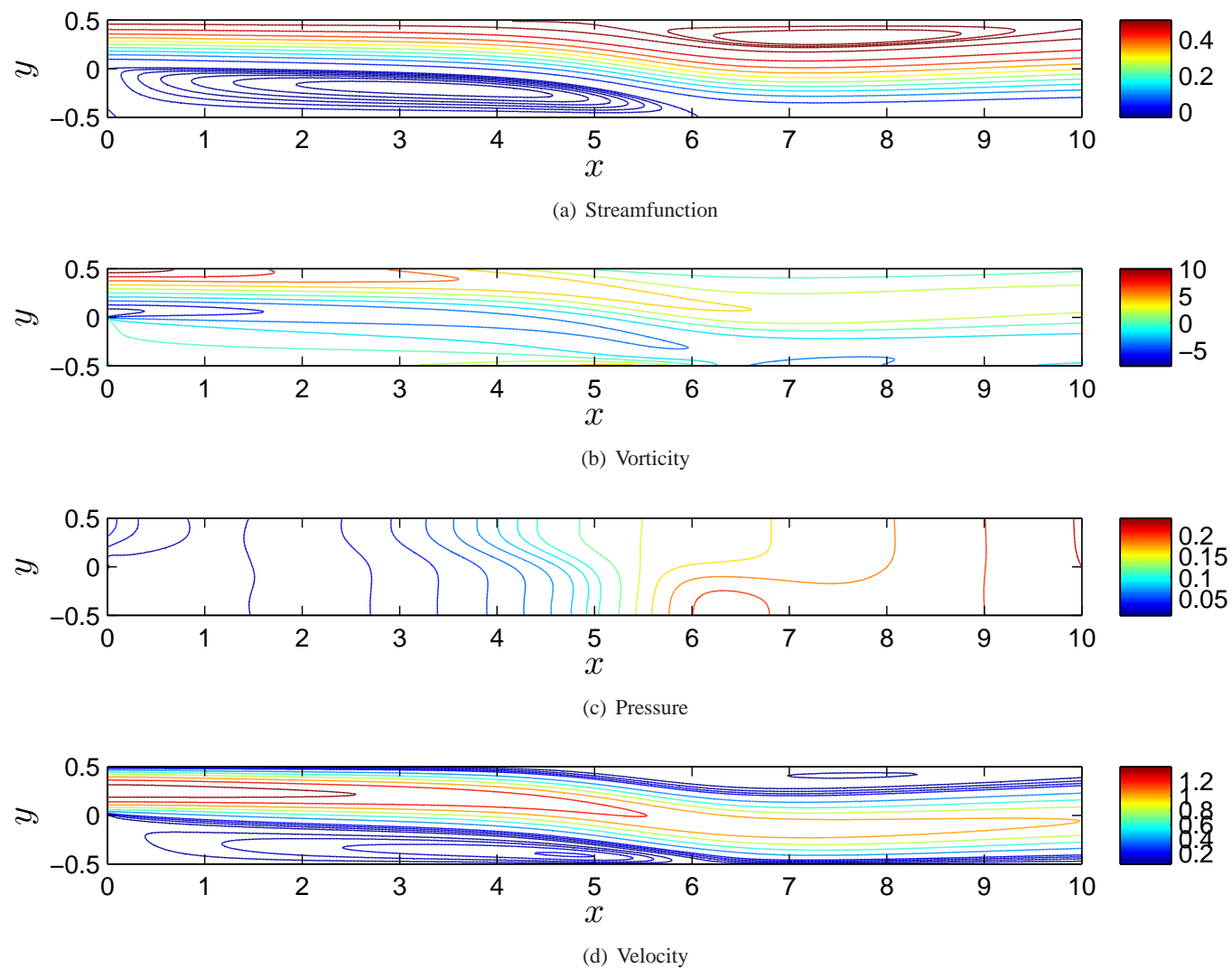


Figure 23: Flow over a backward-facing step, $L = 15$, plots until $x = 10$. For contour line values see [9].

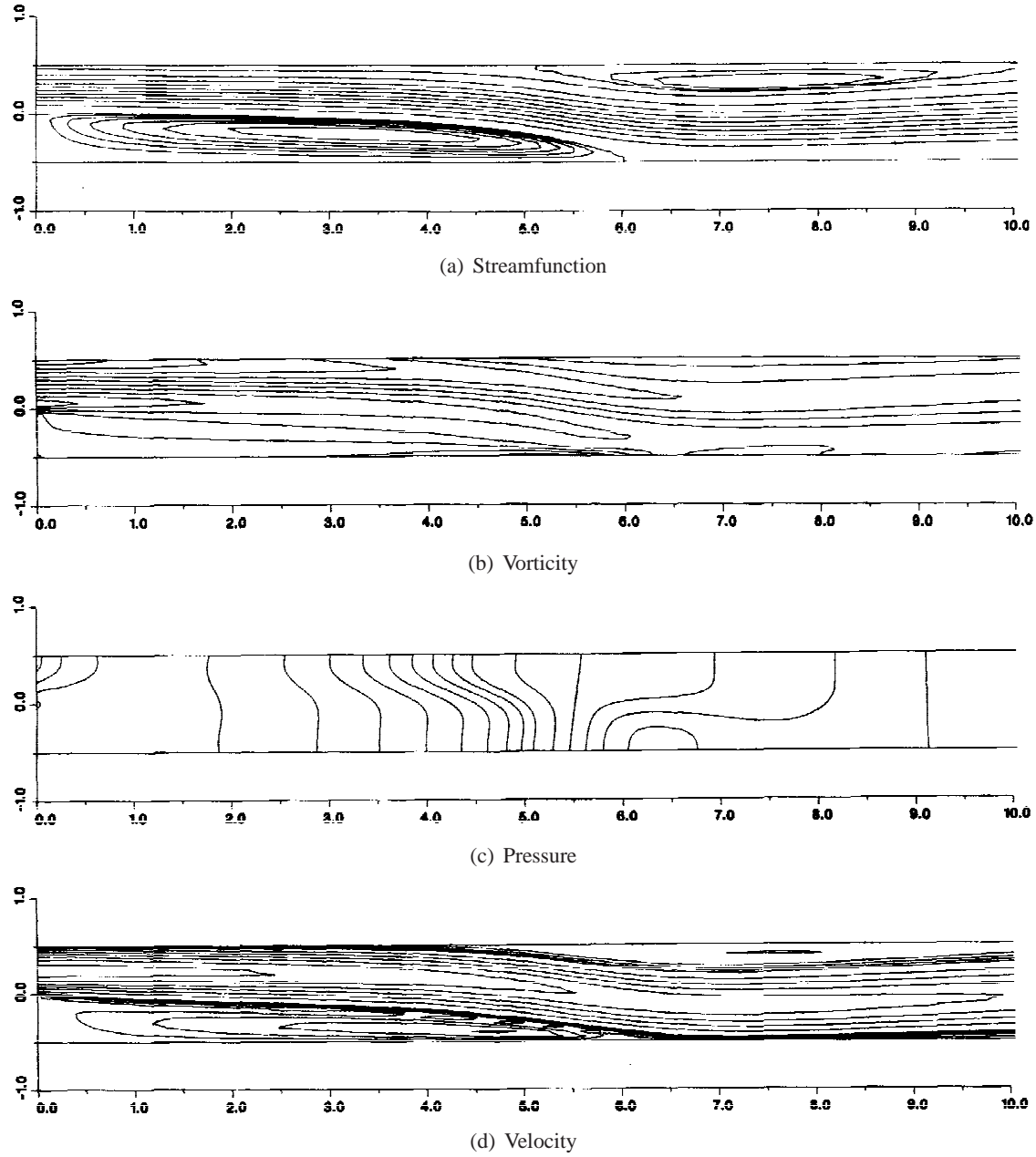
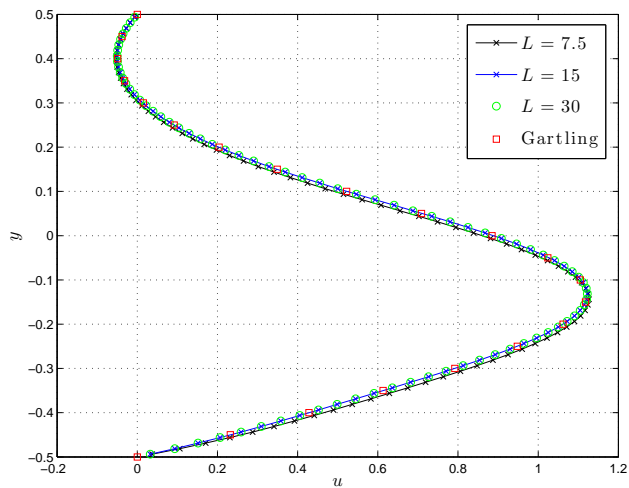
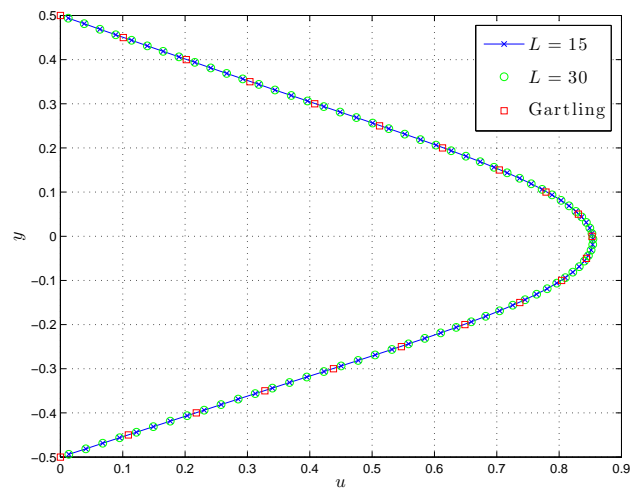


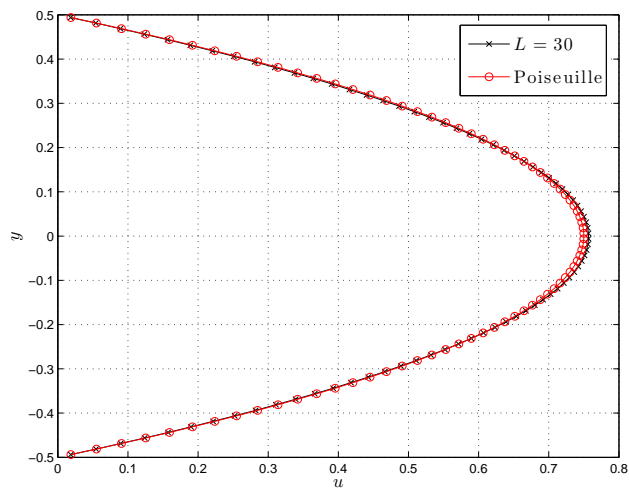
Figure 24: Flow over a backward-facing step, reproduced from [9].



(a) $x = 7$



(b) $x = 15$



(c) $x = 30$

Figure 25: u -velocity profiles for backward-facing step flow.

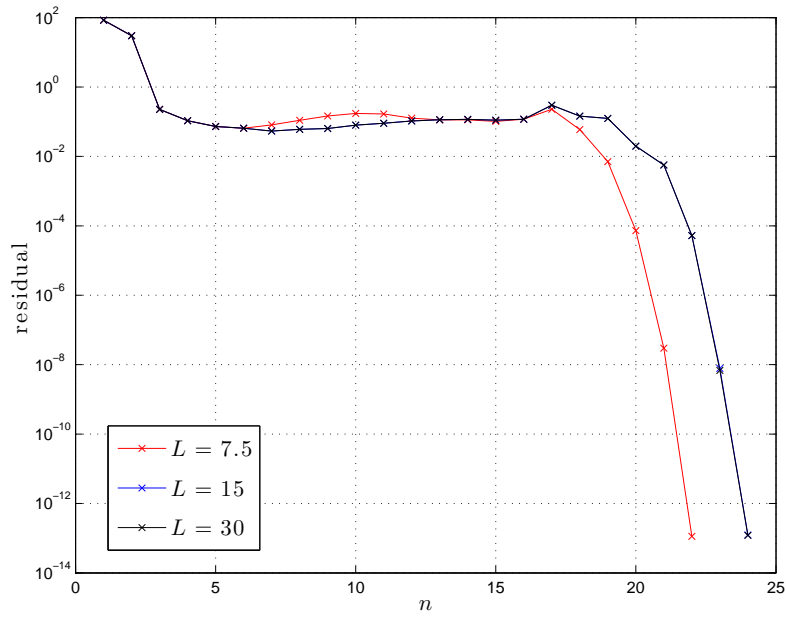


Figure 26: Convergence of residual for different domain sizes for backward-facing step flow.

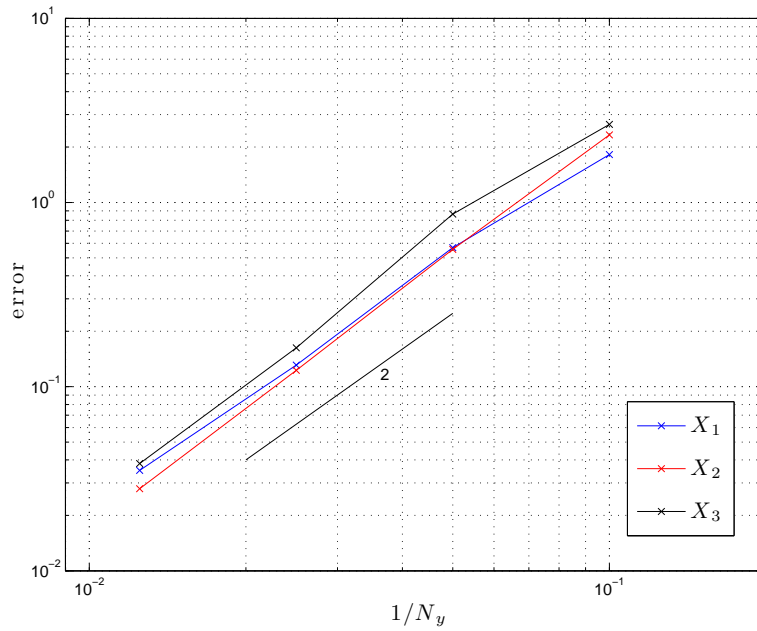


Figure 27: Convergence of error in prediction of recirculation length for backward-facing step flow.

5 Actuator disk model

5.1 Introduction

In order to perform CFD simulations of wind turbine wakes it is common to employ simplified models to represent the turbine [16]. One of these simplified models is the actuator disk, which models the action of the turbine on the flow as a sink of momentum by introducing a forcing term in the Navier-Stokes equations. This force appears as a surface integral in the finite volume formulation of the equations:

$$\int_{\Omega \cap S} \mathbf{f} \, dS. \quad (36)$$

Here \mathbf{f} is the non-dimensional surface force per area, Ω the (finite) volume over which is integrated, and S the surface on which the force acts. Assuming the forcing is in x -direction, i.e. $\mathbf{f} = f_x \hat{\mathbf{e}}_x$, the total force term can be expressed in terms of the thrust coefficient:

$$\int_{\Omega \cap S} f_x \, dS = -\frac{1}{2} C_T A_d. \quad (37)$$

The factor of $\frac{1}{2}$ appears due the definition of C_T and the non-dimensionalization of the force term, which scales with $\rho_\infty u_\infty^2$. The minus sign appears because the force *on the flow* is minus the thrust force on the turbine. A_d is the area of the disk with radius R . In a discrete sense equation (37) changes into a summation over finite volumes, so we obtain for a force in x -direction:

$$\sum_j f_{x_j} \Delta y_j = -\frac{1}{2} C_T A_d, \quad (2D: A_d = 2R), \quad (38)$$

$$\sum_{j,k} f_{x_{j,k}} \Delta y_j \Delta z_k = -\frac{1}{2} C_T A_d, \quad (3D: A_d = \pi R^2). \quad (39)$$

For a uniformly loaded actuator disk these simplify to $f_{x_j} = -\frac{1}{2} C_T$ and $f_{x_{j,k}} = -\frac{1}{2} C_T$.

We repeat a number of test cases performed by Réthoré [15] to test our discretization. Comparison will be made with analytical solutions, which are available for 1D, 2D and 3D inviscid flows through actuator disks.

5.2 1D

We start with an actuator disk in 1D. In our staggered arrangement the force f_x acts at the center of a u -centered finite volume. There are no pressure-velocity coupling issues (in contrast to earlier work, e.g. [18], [14], [15]). With symmetry boundary conditions at top and bottom ($\frac{\partial u}{\partial y} = 0$, $v = 0$), outflow boundary conditions ($\frac{\partial u}{\partial x} = 0$, $v = 0$) and f_x independent of y , the flow remains one-dimensional (figure 28, left). From the continuity equation we then see that $\frac{\partial u}{\partial x} = 0$, so $u = \text{constant} = u_\infty$. The momentum equation reduces to

$$\int_{\Gamma} p n_x \, dy = \int_{\Omega \cap S} f_x \, dy, \quad (40)$$

so for uniform f_x this leads to

$$\Delta p = -\frac{1}{2} C_T. \quad (41)$$

It follows that the pressure is constant in the entire domain, except at the point where f_x is non-zero, where the pressure jumps. This jump Δp is equal to $-\frac{1}{2} C_T$, indicating that the pressure drops. The Reynolds number does not play a role here.

In figure 29 the pressure as function of x is shown for two different meshes with 10×10 and 20×20 (the number of volumes in y -direction is not important). The domain is 1×1 and $C_T = \frac{1}{2}$, so that $\Delta p = -\frac{1}{4}$. It can be seen that the analytic solution is exactly captured on both meshes. Note that the solution is obtained after only one iteration because the problem is essentially linear.

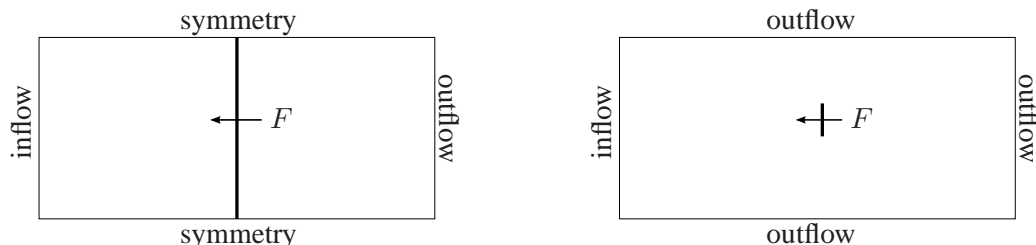


Figure 28: 1D (left) and 2D (right) layout for actuator disk simulations.

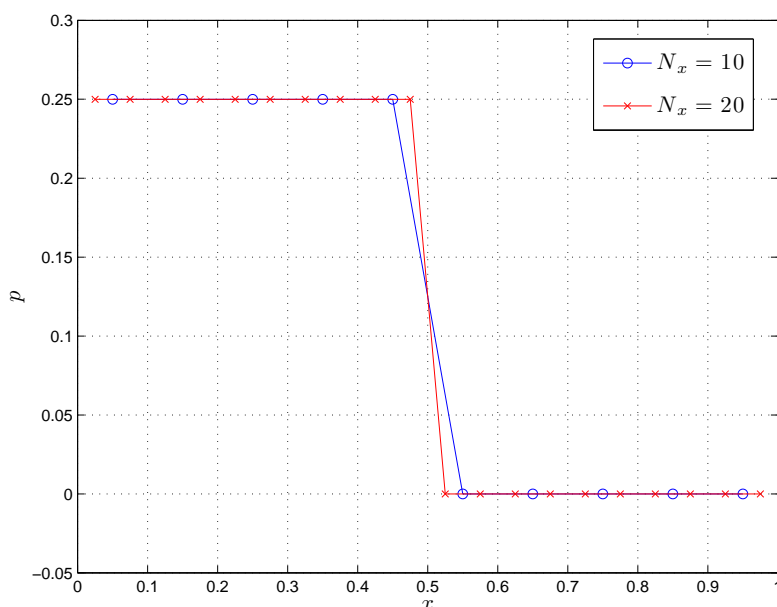


Figure 29: Pressure as function of x for 1D actuator disk.

5.3 2D lightly loaded, ‘inviscid’

5.3.1 Introduction

We will now consider the more physical situation of an actuator disk that spans only part of the domain, see the right graph in figure 28. A uniformly loaded actuator disk presents a challenging test case due to the presence of a singularity at the disk edge, where high gradients appear and vorticity is created. The actuator disk is positioned at $x = 0$ and defined for $|y| < R$. For a lightly loaded actuator disk ($C_T \ll 1$) an analytical solution is available,

$$p = \frac{\Delta p}{2\pi} \left(\tan^{-1} \left(\frac{R-y}{x} \right) + \tan^{-1} \left(\frac{R+y}{x} \right) \right) \quad (\Delta p < 0), \quad (42)$$

$$u = u_\infty - \frac{p}{\rho u_\infty} + \underbrace{\frac{\Delta p}{\rho u_\infty}}_{\text{in the wake}}. \quad (43)$$

‘In the wake’ means $x > 0$ and $|y| < R$. In contrast to previous test cases, where analytical or benchmark results could be used to investigate the order of the spatial discretization, this is more difficult here because:

- The analytical solution requires boundary conditions infinitely far from the actuator disk.
- The analytical solution is valid for the linearized Navier-Stokes equations.
- The analytical solution is valid for inviscid flow.

The analytical solution is therefore not used for order studies, but for qualitative comparison only.

5.3.2 Settings

In order to make a fair comparison with this analytical result the inflow velocity at the left side of the domain is calculated from this equation. We set $C_T = 0.001$ and with a domain of $[-10, 10] \times [-10, 10]$ this leads to $u(-10, 0) \approx 0.999992$. The pressure is determined up to a constant, which is chosen such that $p = 0$ at the center of the actuator disk, corresponding to the analytical solution. The restriction on C_T makes sure that the flow remains almost one-dimensional, but since the width of the domain is now larger than the size of the disk, the flow can decelerate. For such a low C_T the wake velocity u_w (i.e. when $x \rightarrow \infty$) according to expression (43) is $u_w/u_\infty = 1 + \Delta p$. Comparing with quasi 1D momentum theory:

$$u_w/u_\infty = \sqrt{1 - C_T} \approx 1 - \frac{1}{2}C_T \quad (C_T \ll 1), \quad (44)$$

it is observed that the analytical solution satisfies $\Delta p \approx -\frac{1}{2}C_T$, as in the pure 1D case. As boundary conditions we prescribe inflow on the left side and outflow conditions on all other sides, i.e.

$$p - \frac{1}{\text{Re}} \frac{\partial u}{\partial x} = p_\infty \quad \frac{\partial v}{\partial x} = 0 \quad (x = 10), \quad (45)$$

$$p - \frac{1}{\text{Re}} \frac{\partial v}{\partial y} = p_\infty \quad \frac{\partial u}{\partial y} = 0 \quad (y = -10, y = 10), \quad (46)$$

so that the wake can expand and fluid can flow through the upper and lower sides of the domain.

The grid that is used is shown in figure 30. In x -direction the grid is mildly stretched away from the rotor with a stretching factor of 1.01. In y -direction a uniform grid is employed for $|y| < 1$, and outside this region the grid is stretched with a factor of 1.05. We take $\Delta x = \Delta y = 1/30$ at the disk, resulting in a total of 278×168 finite volumes.

The system of equations is solved by starting with 1 step Picard iteration after which Newton iteration converged in 1 or 2 steps to a residual smaller than 10^{-10} in all cases.

5.3.3 Results

Since the analytic solution is valid for inviscid flow, it is strictly not correct to perform viscous simulations. However, since there are no solid boundaries in the flow, there is no presence of a

| parameter | value |
|----------------------|--------------------|
| Re | $10^2, 10^3, 10^4$ |
| C_T | 10^{-3} |
| L | 20 |
| H | 20 |
| R | 1/2 |
| $\Delta x, \Delta y$ | 1/30 |

Table 7: Settings for lightly loaded 2D actuator disk.

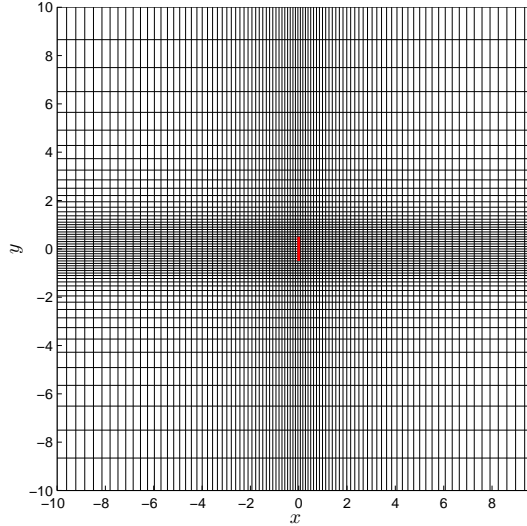


Figure 30: Mesh used for simulations. Every third grid line is shown.

boundary layer which changes significantly with Reynolds number. The flow through the centerline of the disk is smoothly varying, making $\frac{\partial^2 u}{\partial x^2}$ very small. Only at the edges of the disk, where vorticity is created, diffusion acts to smear out the velocity and vorticity. As long as the Reynolds number attains a minimum value, the velocity at the centerline will hardly be affected [19]. In this case this minimum Reynolds number will be even smaller than reported in [19], because we are working with a C_T of 0.001, at which very little vorticity is produced.

Figures 31 and 32 show the pressure and velocity through the centerline of the actuator disk. In all cases we plot the deviation of the freestream velocity, Δu , normalized by the pressure jump Δp . The pressure is also normalized by Δp . This gives values between -1 and 0 for the velocity and between -0.5 and 0.5 for the pressure. We note the following:

- The pressure is almost completely independent of the Reynolds number. The agreement with the exact (analytical) expression is very good and the pressure jump over the disk is captured perfectly. Only in the wake a small difference in pressure is observed. This is attributed to the fact that at the outflow boundary the pressure is prescribed, and at the inflow the velocity. This leads to a small asymmetry, which is not present in the exact solution.
- The velocity shows a greater sensitivity to the Reynolds number. For $Re = 100$ we see that for $x > 1$ the results deviate from the exact solution. In this case the diffusive term $\frac{1}{Re} \frac{\partial^2 u}{\partial y^2}$ at the edge of the wake is so large that the core of the wake ‘mixes’ with the outer flow. For a higher Reynolds number this term is small enough to make it negligible over the distances we consider. However, when looking at the velocity as function of y at $x \approx 1D$

we see more clearly the dependence on Reynolds number in capturing the sharp interface.

- Careful inspection of the velocity and vorticity upstream of the disk reveals the presence of small oscillations (wiggles) in the solution (see figures 33(b) and 35(b)). With central discretizations a *sufficient* condition to avoid wiggles is to have a mesh Péclet number smaller than 2, i.e. $h \leq 2/\text{Re}$. This criterion is met near the disk for $\text{Re} = 100$, but not for $\text{Re} = 1000$ and 10000 , so that the presence of wiggles is not surprising. Their effect remains small and restricted to the flow region where high gradients appear, indicating that the mesh Péclet condition is not always a *necessary* condition, especially when the gradients are not in the direction of the flow.

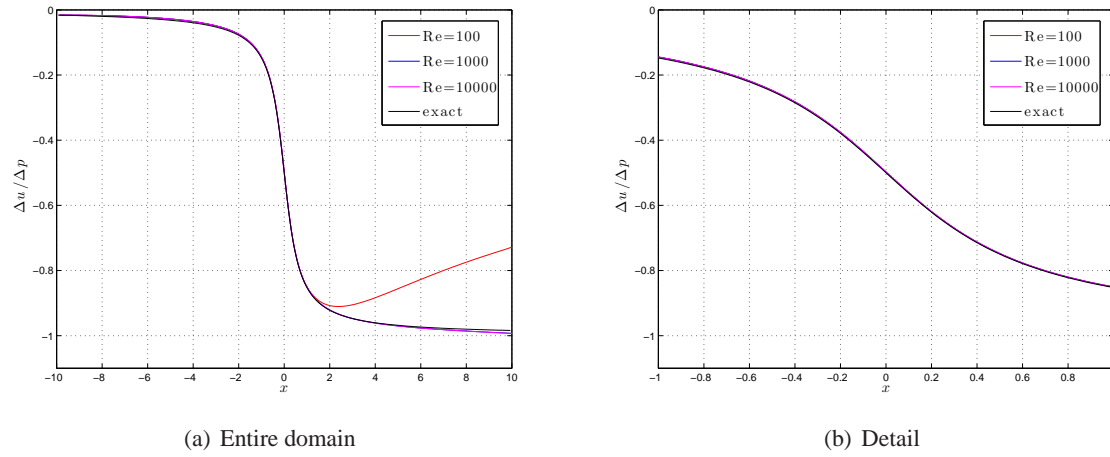


Figure 31: u -velocity through centerline of actuator disk for different Reynolds numbers.

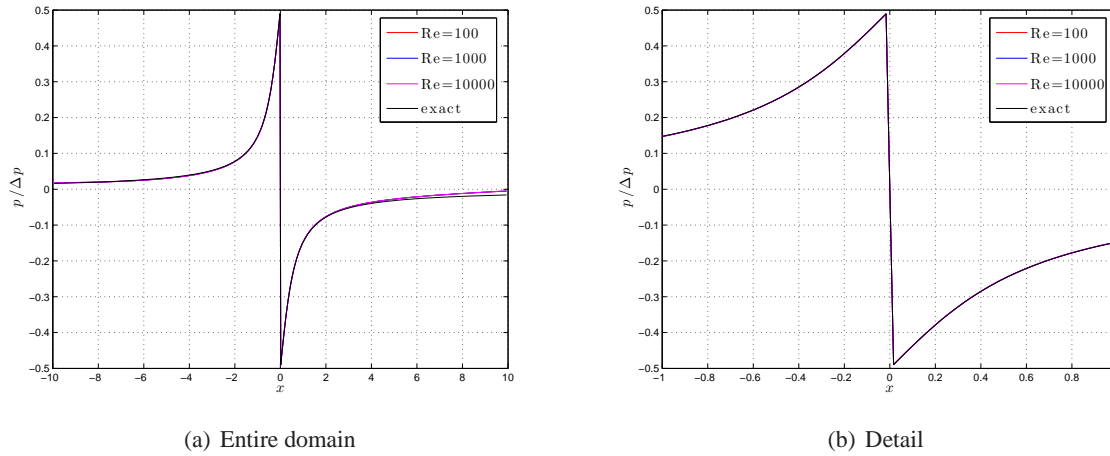
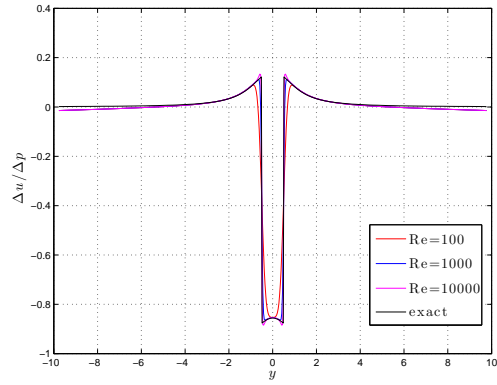
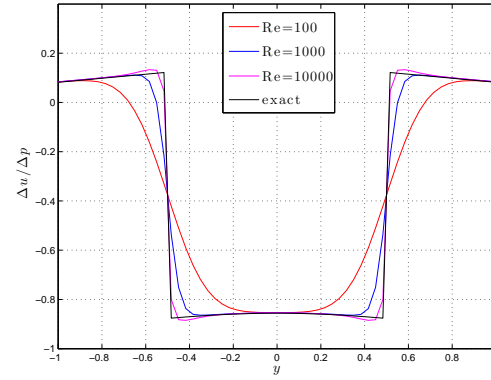


Figure 32: Pressure through centerline of actuator disk for different Reynolds numbers.

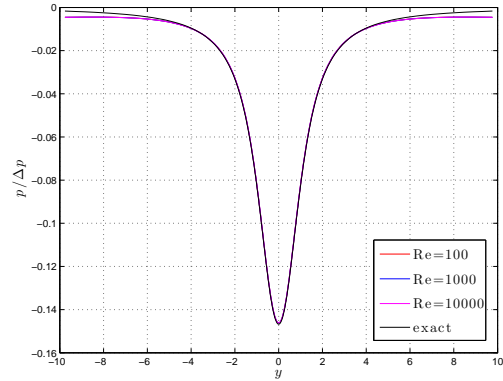


(a) Entire domain

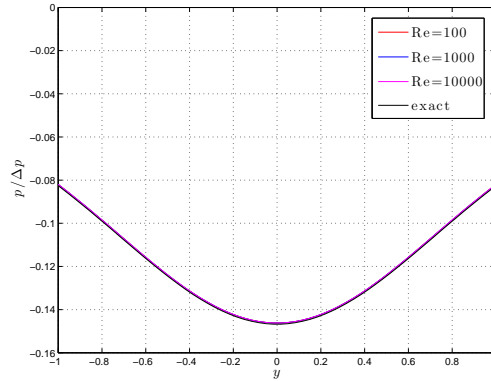


(b) Detail

Figure 33: u -velocity as function of y at $x \approx 1D$ for different Reynolds numbers.



(a) Entire domain



(b) Detail

Figure 34: p as function of y at $x \approx 1D$ for different Reynolds numbers.

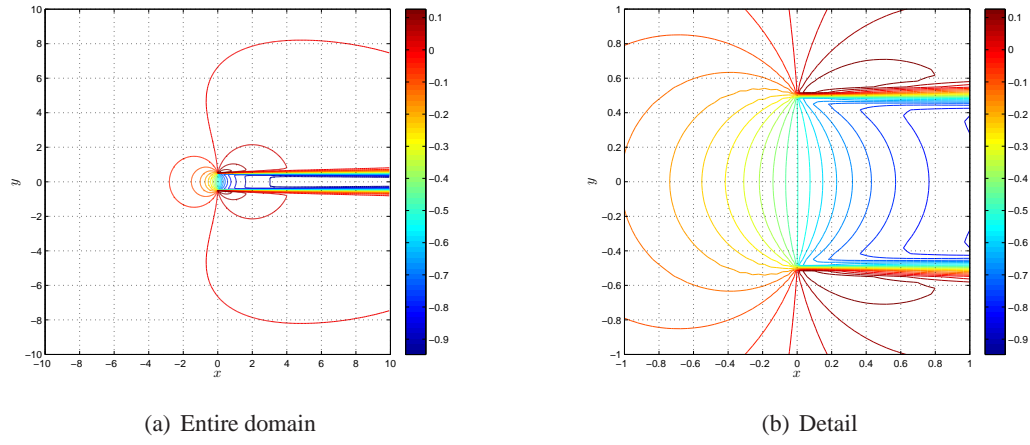


Figure 35: Velocity contours ($\Delta u/\Delta p$) at $Re = 1000$.

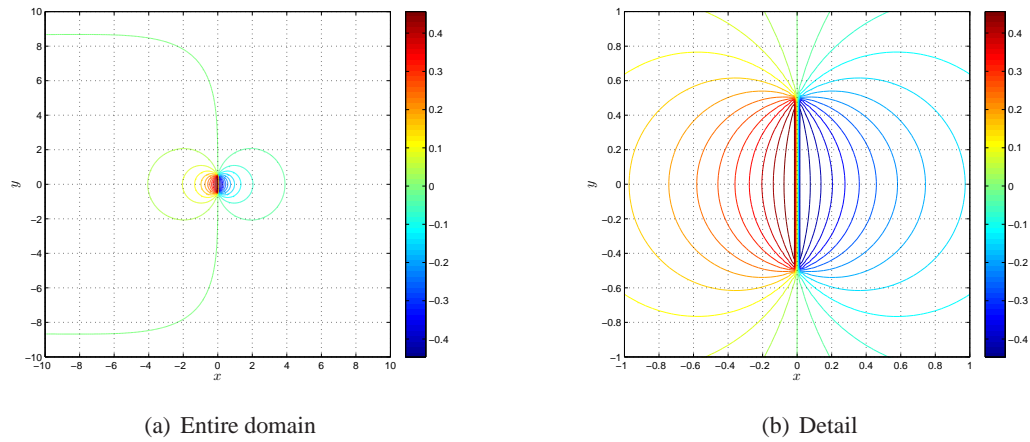


Figure 36: Pressure contours ($p/\Delta p$) at $Re = 1000$.

5.4 2D heavily loaded, ‘inviscid’

A physically more interesting example is obtained when taking $C_T = 0.8$. The gradients in the flow are stronger and it is more important to satisfy the mesh Péclet condition. To save on the mesh requirements the stretching factors have been increased to 1.03 and 1.1, in x - and y -direction respectively. The Reynolds number is $\text{Re} = 1000$, which was shown to be high enough for viscous effects to be small. Figures 37(a) and 37(b) show the vorticity field for a ‘coarse’ mesh with $\Delta x = 1/100$, $\Delta y = 1/100$ (total 232×294), and a ‘fine’ one with $\Delta x = 1/600$ and $\Delta y = 1/100$ (total 350×294). The wiggles in x -direction disappear on the fine mesh because the mesh Péclet condition is satisfied at the actuator disk. However, the uniform actuator force that is used here leads to a singular vorticity at the edges of the disk and does not converge to a finite value upon mesh refinement.

The streamlines obtained with this mesh are shown in figure 38, clearly displaying the expansion of the flow. The convergence of the residual now takes approximately 6 iterations.

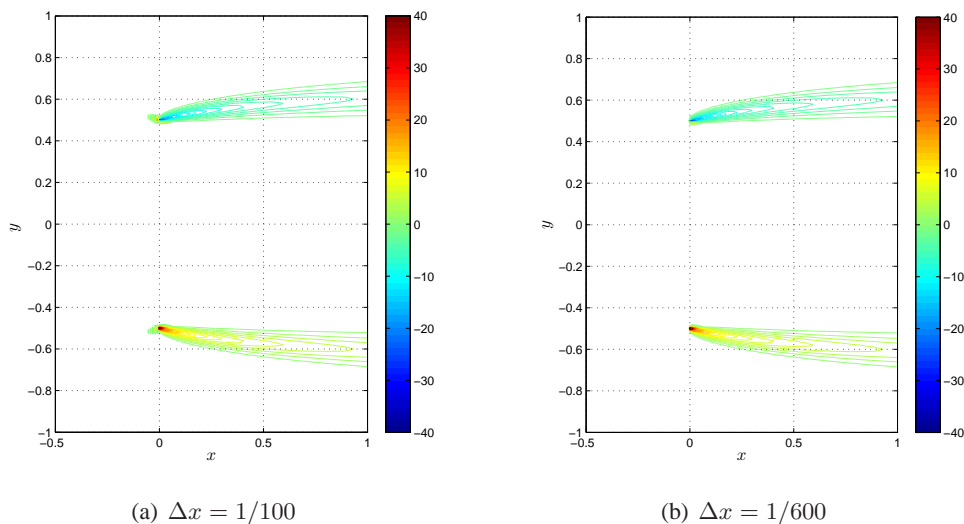


Figure 37: Vorticity contours at $C_T = 0.8$ and $\text{Re} = 1000$.

5.5 2D heavily loaded, viscous

The previous test is not very suitable for investigating the order of accuracy, because a fine mesh is already required to obtain an oscillation-free result. We therefore take a lower Reynolds number, $\text{Re} = 10$, so that the mesh Péclet condition is already satisfied for $h < 2/10$. Furthermore we use a smaller domain with symmetry boundary conditions on the lower and upper side; the corresponding Dirichlet conditions for v lead to a faster convergence of the residual. The maximum residual converges in four steps (1 Picard and 3 Newton) to a value lower than 10^{-10} .

| parameter | value |
|----------------------|-------------------|
| Re | 10 |
| C_T | 0.8 |
| L | 4 |
| H | 4 |
| R | 1/2 |
| $\Delta x, \Delta y$ | 1/4, 1/8... 1/128 |

Table 8: Settings for heavily loaded viscous 2D actuator disk.

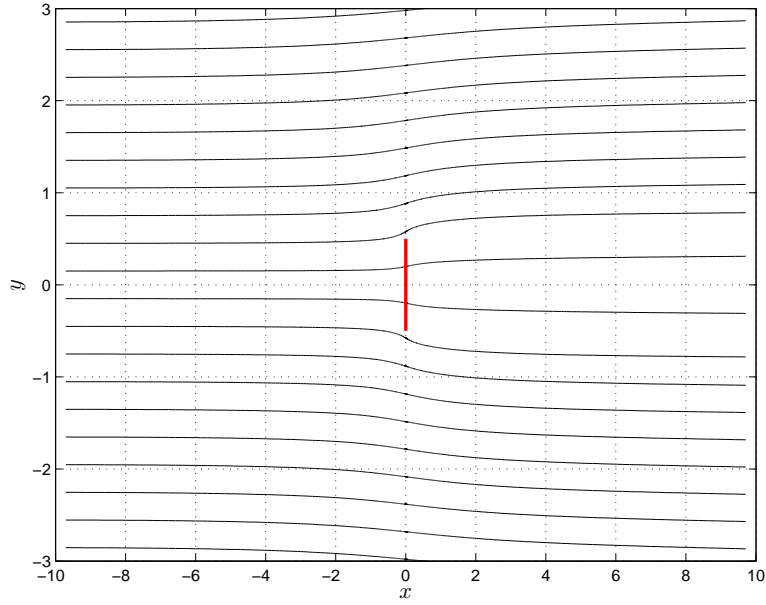


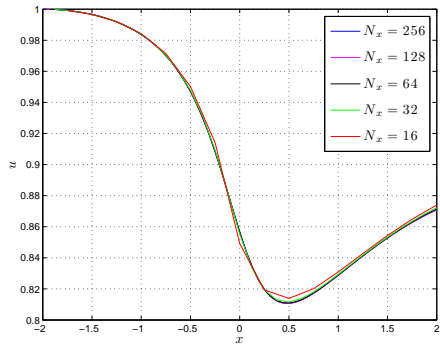
Figure 38: Streamlines through actuator disk for $C_T = 0.8$, $\text{Re} = 1000$.

Figures 39(a)-39(e) show the evolution of velocity and pressure profiles across different cross sections upon mesh refinement, either along $y = 0$ or $x = 1$. It is observed that the pressure and vertical velocity need a relatively fine mesh to obtain ‘mesh independent’ results. This is probably due to the fact that the pressure is discontinuous across the disk and the vertical velocity has two distinct sharp peaks at the edges of the disk. The horizontal velocity is, on the contrary, smooth in the entire field (at this Reynolds number).

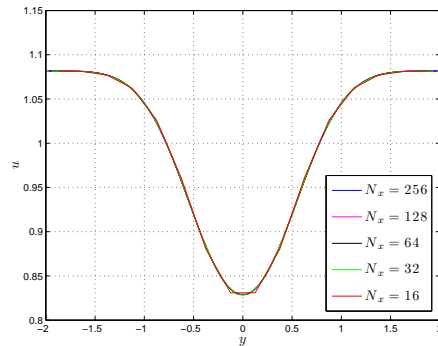
The error in these velocity profiles as function of mesh width is shown in figures 40(a) and 40(b). This error is calculated with respect to a simulation on a fine mesh with 512×512 finite volumes:

$$e = \left(\frac{1}{N} \sum_i^N |\bar{u}_i - u_i^h|^p \right)^{1/p}, \quad (47)$$

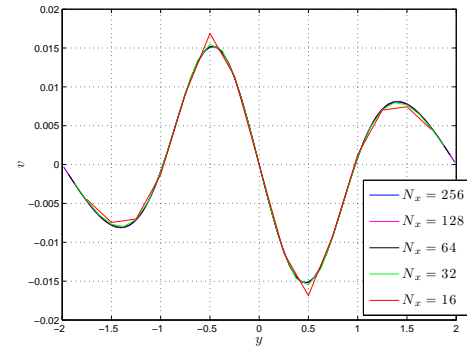
where $p = 2$ or $p = \infty$, u_i^h the solution in point i corresponding to a mesh with spacing h , and \bar{u}_i the solution on the 512×512 mesh *linearly* interpolated (this is important because of the discontinuity) to the mesh locations corresponding with spacing h . The second order accuracy of the spatial discretization, shown in all previous test cases, is not so clear here. Both velocity and pressure show convergence rates between 1 and 2, generally around 1.6. In all cases the L_∞ -norm shows larger errors than the L_2 -norm, as expected, but the rate of convergence is the same for both. The error in total energy changes from second to third order around $h = 10^{-2}$; we do not have an explanation for this yet.



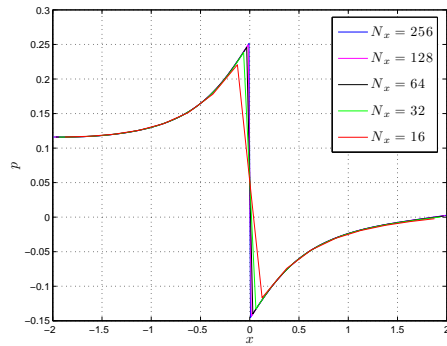
(a) $u - x$



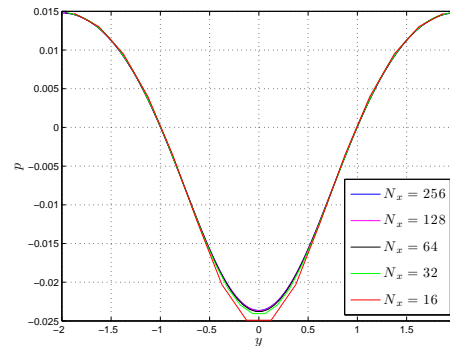
(b) $u - y$



(c) $v - y$

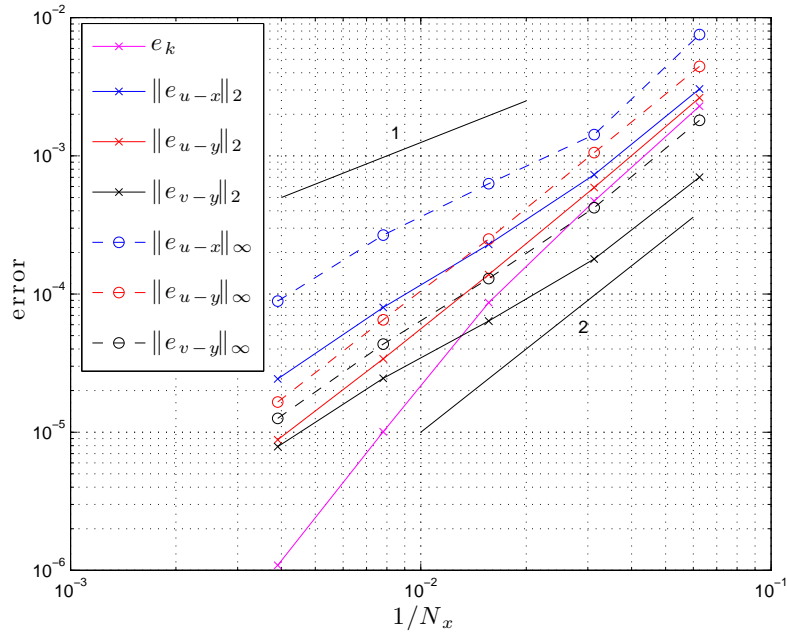


(d) $p - x$

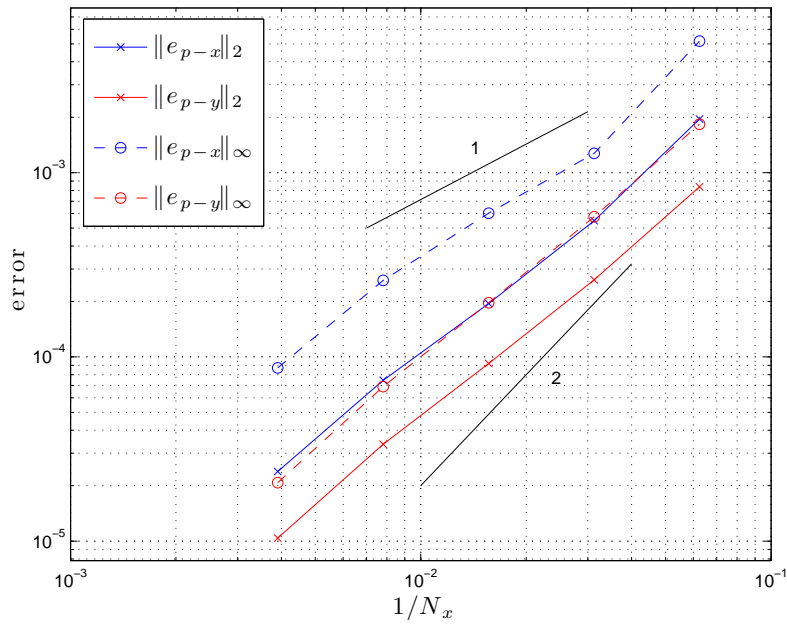


(e) $p - y$

Figure 39: Velocity and pressure profiles for different meshes for 2D actuator disk. $C_T = 0.8$, $Re = 10$.



(a) Velocity



(b) Pressure

Figure 40: Mesh convergence study for 2D actuator disk. $C_T = 0.8$, $Re = 10$.

5.6 3D lightly loaded

5.6.1 Introduction

In the three-dimensional case again an analytic solution is available for lightly loaded actuator disks ($C_T \ll 1$):

$$p(x, r, \theta) = \frac{\Delta p}{4\pi} \int_0^R \int_0^{2\pi} \frac{\tilde{r} x}{\left(\tilde{r}^2 + r^2 + x^2 - 2\tilde{r}r \cos(\tilde{\theta} - \theta)\right)^{3/2}} d\tilde{r} d\tilde{\theta}. \quad (48)$$

Along the centerline of the disk ($r = 0$) this equation can be exactly integrated:

$$p(x) = \frac{\Delta p}{2} \int_0^R \frac{\tilde{r} x}{(\tilde{r}^2 + x^2)^{3/2}} d\tilde{r} = \left[\frac{-\Delta p}{2} \frac{x}{\sqrt{x^2 + r^2}} \right]_{r=0}^{r=R}. \quad (49)$$

The velocity follows as in 2D from (43), and satisfies again $u_w/u_\infty = 1 + \Delta p$, with $\Delta p = -\frac{1}{2}C_T$. The 2D and 3D solutions are qualitatively different, see for example the centerline pressure and velocity profiles in figure 41. In 3D the wake expands in a much shorter distance, has a larger velocity deficit at a given downstream position and obtains the asymptotic wake value much faster.

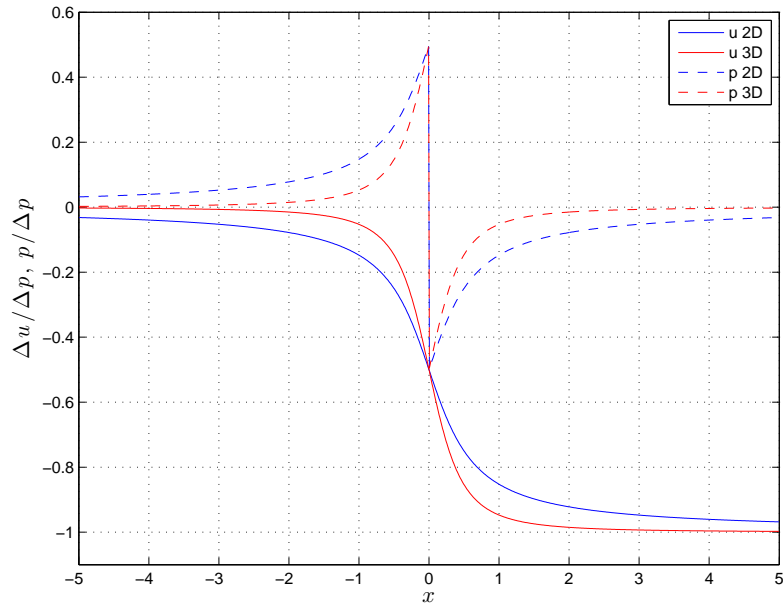


Figure 41: Pressure and velocity in 2D and 3D along centerline according to analytical solutions.

To model the circular actuator disk in our Cartesian mesh we do the following. For each volume (i, j, k) we calculate the area $A_{i,j,k}$ that is covered by the actuator disk. For a uniformly loaded disk the forcing on each cell is then simply $\frac{1}{2}C_T A_{i,j,k}$. Figure 42 shows how the forcing is distributed in the $y - z$ plane at $x = 0$. This approach introduces an additional error (see the list in section 5.3) in approximating the analytic solution.

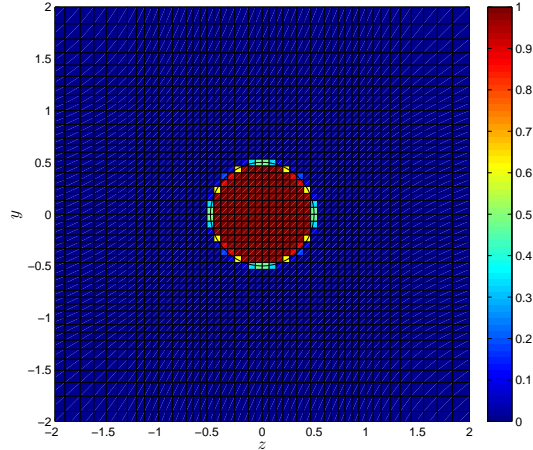


Figure 42: Fraction of volumes covered by actuator disk.

5.6.2 Settings

Because the velocity and pressure recover faster to the asymptotic upstream and downstream values in 3D than in 2D, we use a smaller domain for the 3D simulations, being $12 \times 8 \times 8$, and prescribe $u = 1$ on the inflow boundary. The grid stretching is 1.02 in x -direction and 1.1 in y - and z -directions (for $|y|, |z| > 1$), resulting in a total of $102 \times 64 \times 64$ finite volumes. Based on the 2D study we use a Reynolds number of 1000 and a C_T of 0.001.

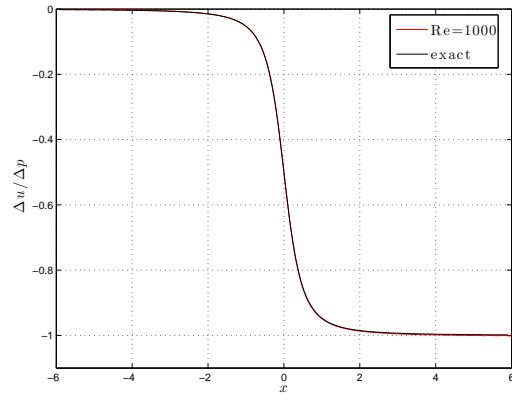
In contrast to all previous test cases, the steady state solution for this test is obtained by marching in time with a classical explicit four-stage Runge-Kutta method with (only) one pressure correction per time step. One pressure correction step reduces the temporal accuracy of the velocity (to second order), but the linear stability region is not affected, which is more important when marching to steady solutions. The Poisson equation for the pressure is solved with a preconditioned conjugate gradient method. The time step is determined by estimating the possible eigenvalues of the convection and diffusion matrices with Gershgorin's theorem, and requiring that the largest possible eigenvalue lies within the stability domain of the Runge-Kutta method. The stopping criterion is 10^{-8} based on the maximum residual.

| parameter | value |
|----------------------|-----------|
| Re | 10^3 |
| C_T | 10^{-3} |
| L | 12 |
| H | 8 |
| D | 8 |
| R | 1/2 |
| $\Delta x, \Delta y$ | 1/15 |

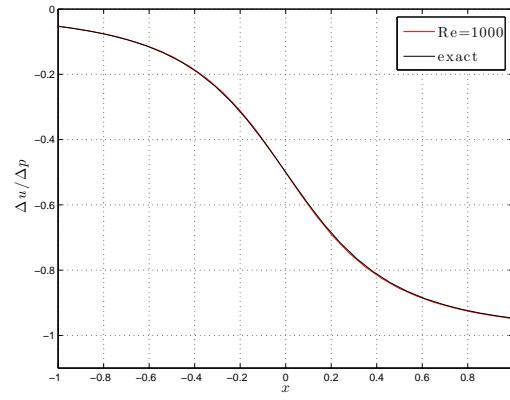
Table 9: Settings for lightly loaded 3D actuator disk.

5.6.3 Results

Figures 43-46 show the velocity and pressure profiles in x - and y -direction along $y = 0$ and $x \approx 1$, respectively. Like in 2D we see excellent agreement with the exact analytical solution. Close inspection of u near $x = -5$ reveals the presence of small wiggles, but they hardly influence the overall velocity and pressure profiles.

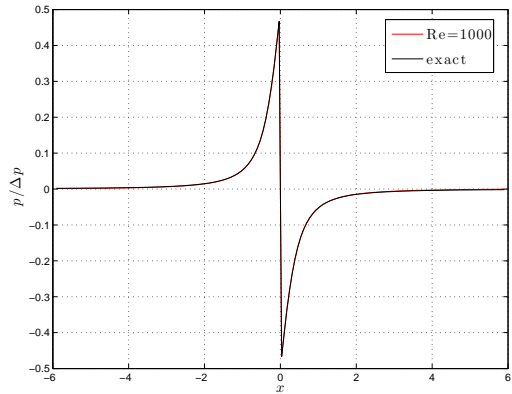


(a) Entire domain

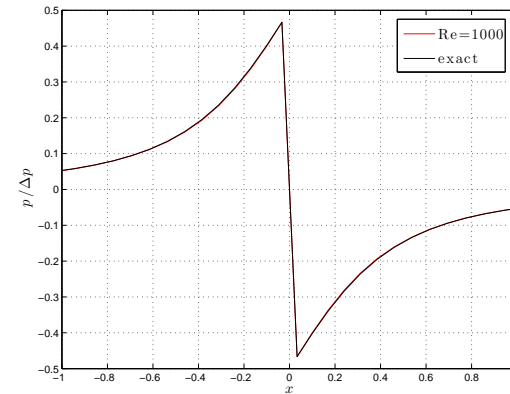


(b) Detail

Figure 43: u -velocity through centerline of actuator disk.

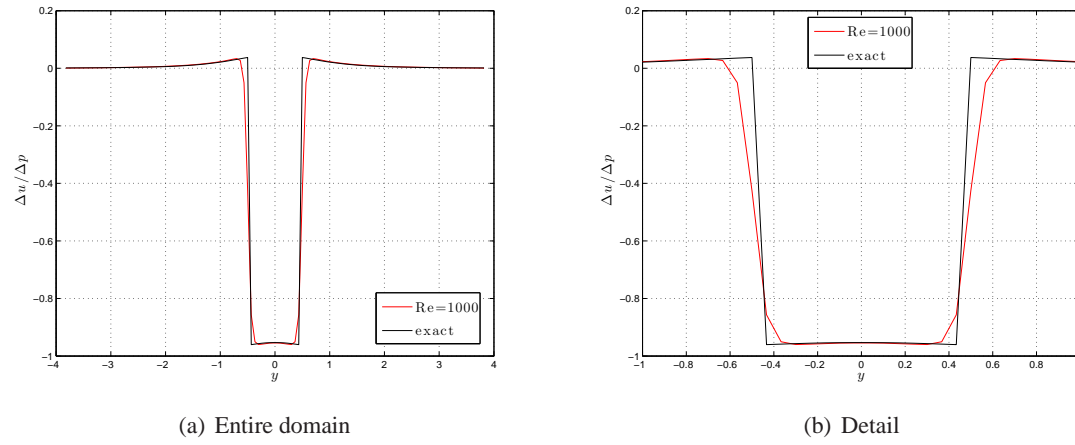
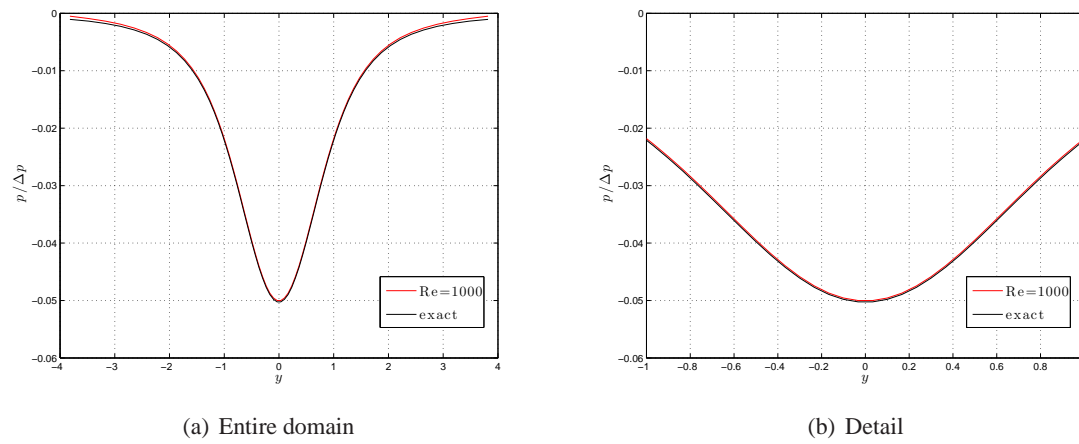


(a) Entire domain



(b) Detail

Figure 44: Pressure through centerline of actuator disk.

Figure 45: u -velocity as function of y at $x \approx 1D$.Figure 46: p as function of y at $x \approx 1D$.

5.7 3D heavily loaded, viscous

5.7.1 Introduction

Similar to section 5.5 we do a simulation with a realistic thrust coefficient, $C_T = 0.8$, and a low Reynolds number, $Re = 10$, in order to do a mesh convergence study.

5.7.2 Settings

We use symmetry boundary conditions at the upper, lower, front and back side to increase the convergence speed, as before. The grids range from 8^3 to 64^3 on a domain of $4 \times 4 \times 4$.

| parameter | value |
|----------------------|----------------|
| Re | 10 |
| C_T | 0.8 |
| L | 4 |
| H | 4 |
| D | 4 |
| R | 1/2 |
| $\Delta x, \Delta y$ | 1/2, ..., 1/16 |

Table 10: Settings for heavily loaded viscous 3D actuator disk.

5.7.3 Results

Figures 47(a)-47(e) show the velocity and pressure profiles for the sequence of meshes mentioned above. Note that the pressure is shifted and scaled by Δp . In all cases we observe a clear convergence towards a mesh independent result. The velocity deficit directly behind the disk is larger than in 2D, but due to a faster recovery of the wake the deficit at $x = 2$ is smaller than in 2D.

The error in the velocity profiles is calculated in the same way as equation (47), where the reference results are now on the 64^3 mesh. The order of accuracy is second order in all cases, for both L_2 - and L_∞ - norms. However, we should keep in mind that the range of grid sizes is quite limited here, and in 2D order reduction was observed for finer grids. Surprisingly the kinetic energy of the flow shows a much larger error constant than in the 2D test; this might be due to the additional error introduced by representing the circular actuator disk on a Cartesian mesh.

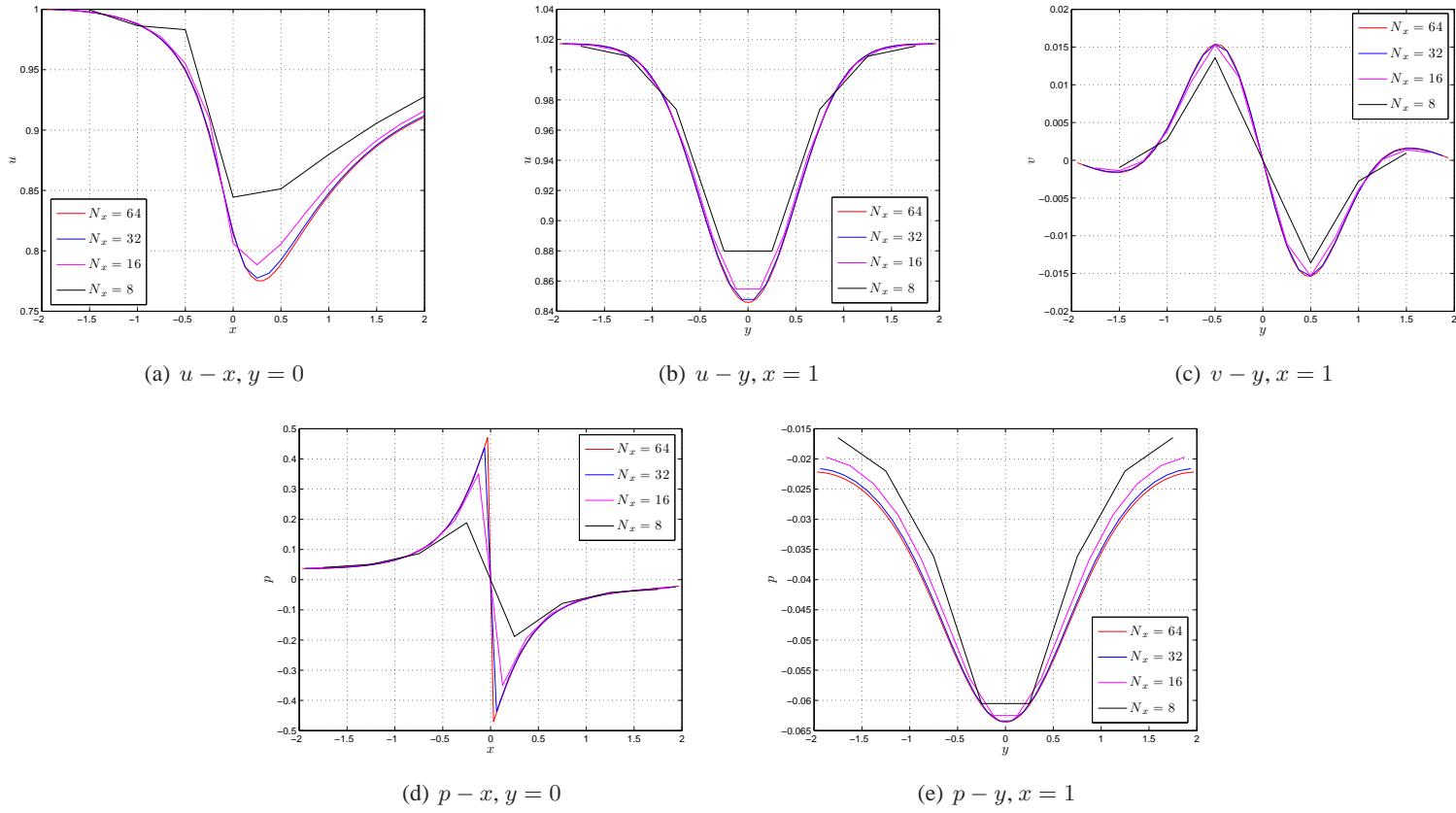
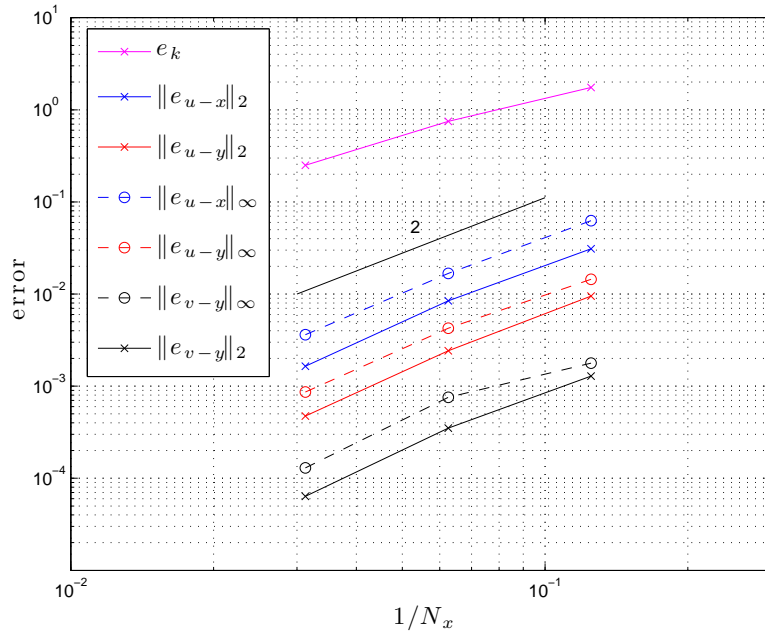
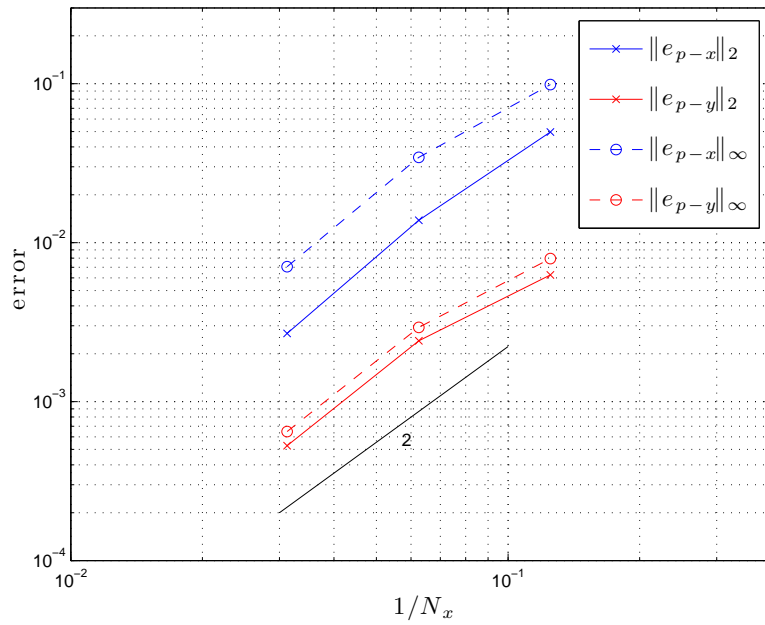


Figure 47: Velocity and pressure profiles for different meshes for 3D actuator disk. $C_T = 0.8$, $Re = 10$.



(a) Velocity



(b) Pressure

Figure 48: Mesh convergence study for 3D actuator disk. $C_T = 0.8$, $\text{Re} = 10$.

6 Conclusions

This report verifies a staggered incompressible Navier-Stokes code in solving a number of steady laminar flow problems. The second order spatial accuracy of this code has been shown by performing thorough grid refinement studies for various flow problems in two and three dimensions: Couette and Poiseuille flow, flow in a lid-driven cavity, flow over a backward-facing step and flow through an actuator disk. We conclude the following:

- The velocity and pressure are second order accurate in space for all flow problems, except for the actuator disk problem, where the accuracy lies between first and second order. This is attributed to the non-smoothness of the pressure and velocity field.
- Second order accuracy has been shown on both uniform and non-uniform grids, where the latter were taken as smooth transformations of a uniform grid. For non-smooth grids, e.g. of Shishkin type, mesh convergence studies were not performed, but second order accuracy is still expected (see e.g. [21, 8]).
- Second order accuracy holds for all boundary conditions investigated, being no-slip, symmetry, outflow (pressure) and periodic. The outflow boundary condition has been shown to work very effectively for the backward-facing step problem, where it was possible to capture a recirculation bubble at the outflow boundary.
- The staggered grid approach correctly captures the discontinuous pressure behavior across the actuator disk, without having pressure-velocity decoupling issues.
- Since central differences are used for approximation of the convective terms, wiggles can appear when the mesh Péclet number is greater than 2. Satisfying the mesh Péclet condition is a sufficient condition to prevent wiggles, but not always necessary. It is important to satisfy it when large gradients in the direction of the local flow are present. In many cases, such as the lid-driven cavity flow (where the largest gradients appear normal to the flow (boundary layers)), very good results are obtained without strictly satisfying the Péclet condition. This is important, because in many practical (turbulent) flows the viscosity is often very small, so that satisfying the Péclet condition in the entire flow would lead to enormous mesh requirements.
- The solution of the non-linear saddle-point system of equations is efficiently solved with Picard and Newton iterations. Picard iterations are effective to provide a good initial guess for the Newton iteration. Faster convergence is obtained when the Péclet condition is satisfied. The number of Picard iterations necessary for a sufficiently accurate guess has been obtained by trial and error; this could possibly be automated by prescribing a certain drop in residual before switching to Newton. The total number of required iterations for convergence is insensitive to the number of finite volumes. In three dimensions the solution of the entire saddle-point system becomes too expensive, and we have switched to a time-marching method to obtain steady-state solutions. Other approaches are possibly more efficient [2].

Some benefits of the current staggered, energy-conserving approach became already clear in the steady actuator disk test case. However, the real advantages of this approach will manifest themselves in the simulation of *unsteady, turbulent flows*, such as the flow of air through wind turbines in wind farms. The verification and validation of such unsteady flows will be addressed in future work.

References

- [1] S. Albensoeder and H.C. Kuhlmann. Accurate three-dimensional lid-driven cavity flow. *Journal of Computational Physics*, 206:536–558, 2005.
- [2] M. Benzi, G.H. Golub, and J. Liesen. Numerical solution of saddle point problems. *Acta Numerica*, 14:1–137, 2005.
- [3] O. Botella and R. Peyret. Benchmark spectral results on the lid-driven cavity flow. *Computers & Fluids*, 27(4):421–433, 1998.
- [4] C.-H. Bruneau and M. Saad. The 2D lid-driven cavity problem revisited. *Computers & Fluids*, 35:326–348, 2006.
- [5] E. Erturk. Numerical solutions of 2-D steady incompressible flow over a backward-facing step, part I: High Reynolds number solutions. *Computers & Fluids*, 37:633–655, 2008.
- [6] E. Erturk. Discussions on driven cavity flow. *International Journal for Numerical Methods in Fluids*, 60:275–294, 2009.
- [7] E. Erturk, T.C. Corke, and C. Gökçöl. Numerical solutions of 2-D steady incompressible driven cavity flow at high Reynolds numbers. *International Journal for Numerical Methods in Fluids*, 48:747–774, 2005.
- [8] J.H. Ferziger and M. Perić. *Computational Methods for Fluid Dynamics*. Springer, 2002.
- [9] D.K. Gartling. A test problem for outflow boundary conditions – flow over a backward-facing step. *International Journal for Numerical Methods in Fluids*, 11:953–967, 1990.
- [10] U. Ghia, K.N. Ghia, and C.T. Shin. High-Re solutions for incompressible flow using the Navier-Stokes equations and a multigrid method. *Journal of Computational Physics*, 48:378–411, 1982.
- [11] P.M. Gresho, D.K. Gartling, J.R. Torczynski, K.A. Cliffe, K.H. Winters, T.J. Garratt, A. Spence, and J.W. Goodrich. Is the steady viscous incompressible two-dimensional flow over a backward-facing step at $Re = 800$ stable? *International Journal for Numerical Methods in Fluids*, 17:501–541, 1993.
- [12] F.H. Harlow and J.E. Welch. Numerical calculation of time-dependent viscous incompressible flow of fluid with free surface. *Physics of Fluids*, 8:2182–9, 1965.
- [13] W. Hundsdorfer and J. Verwer. *Numerical solution of time-dependent advection-diffusion-reaction equations*. Springer, 2003.
- [14] C. Masson, A. Smaïli, and C. Leclerc. Aerodynamic analysis of HAWTs operating in unsteady conditions. *Wind Energy*, 4:1–22, 2001.
- [15] P.-E. Réthoré and N.N. Sørensen. Actuator disc model using a modified Rhie-Chow/SIMPLE pressure correction algorithm. Comparison with analytical solutions. In *European Wind Energy Conference, Brussels*, 2008.
- [16] B. Sandeise, S.P. van der Pijl, and B. Koren. Review of computational fluid dynamics for wind turbine wake aerodynamics. *Wind Energy*, 2011. In press.
- [17] T.M. Shih, C.H. Tan, and B.C. Hwang. Effects of grid staggering on numerical schemes. *International Journal for Numerical Methods in Fluids*, 9:192–212, 1989.

- [18] J.N. Sørensen and A. Myken. Unsteady actuator disc model for horizontal axis wind turbines. *Journal of Wind Engineering and Industrial Aerodynamics*, 39:139–149, 1992.
- [19] J.N. Sørensen, W.Z. Shen, and X. Munduate. Analysis of wake states by a full-field actuator disc model. *Wind Energy*, 1:73–88, 1998.
- [20] R.W.C.P. Verstappen and A.E.P. Veldman. Symmetry-preserving discretization of turbulent flow. *Journal of Computational Physics*, 187:343–368, 2003.
- [21] P. Wesseling. *Principles of Computational Fluid Dynamics*. Springer, 2001.